ELSEVIER

Efficient Monte Carlo sampling by direct flattening of free energy barriers

Gerhard Besold *, Jens Risbo [1], Ole G. Mouritsen

Membrane and Statistical Physics Group (MEMPHYS), Department of Chemistry, Technical University of Denmark, DTU 207, DK–2800, Lyngby, Denmark

Abstract

Systems undergoing first-order phase transitions are accompanied by free energy barriers which separate the free energy minima characterizing the co-existing phases. These barriers grows with increasing system size. With conventional Monte Carlo simulation methods the characteristic time for crossing the barriers grows exponentially with system size and the system will necessarily get trapped in one of the free energy minima. In order to escape from this trapping, various novel simulation schemes (e.g., multicanonical/multimagnetical sampling, entropic sampling and simulated tempering) have been proposed and successfully applied to model systems. All these methods combine an iterative scheme with histogram reweighting techniques. We apply here another variant of these methods, which involves the use of *shape functions*, which are added to the model Hamiltonian in order to level out the free energy barriers. One of the virtues of this approach is the transparent formulation of the common philosophy underlying all the different so-called 'non-Boltzmann' simulational schemes devised to overcome free energy barriers. The basic principles of the method are presented. The easy adaption of the method to different model systems is demonstrated by application to two case studies, a multi-state lattice model for phase equilibria in a binary lipid bilayer, and a two-dimensional lattice gas model which exhibits interfacial melting, which are known to be notoriously difficult to study by conventional Monte Carlo methods. The practical aspects of the implementation of the method are discussed. The results demonstrate the efficiency and versatility of the shape function method. © 1999 Elsevier Science B.V. All rights reserved.

PACS: 02.70.Lq; 05.70.Fh; 64.60.Cu; 87.15.Da

Keywords: Monte Carlo simulation; Multicanonical sampling; Non-Boltzmann sampling; Histograms; Spectral free energies; Shape functions; Asymmetric first-order phase transitions; Binary lipid bilayers; Interfacial melting

1. Introduction

Monte Carlo (MC) methods are today commonly accepted as an indispensable computer simulation technique for the study of thermal equilibrium properties of many-particle models for condensed matter systems [1–10]. In simulations in the canonical ensemble at temperature T,

---

* Corresponding author. Tel. +45 45 25 24 86; fax: +45 45 93 48 08; e-mail: besold@kemi.dtu.dk

[1] Present address: Department of Dairy and Food Science, The Royal Veterinary and Agricultural University, Bülowsvej 17, DK-1870 Frederiksberg C, Denmark.

microstates of a model system are thereby sampled with the statistical 'Boltzmann weights'

$$\rho_{\mathrm{can}}(E, T) \propto \mathrm{e}^{-\beta E}, \tag{1}$$

where E is the energy of the microstate as determined by the model Hamiltonian, and $\beta = 1/k_{\mathrm{B}}T$ is the inverse temperature. In thermal equilibrium the energy E of the system is a fluctuating quantity, and the canonical probability distribution of energy is given by

$$\mathcal{P}_{\mathrm{can}}(E, T) \propto \Omega(E)\rho_{\mathrm{can}}(E, T) \tag{2}$$

with the density-of-states (degeneracy) $\Omega(E)$. Similar expressions hold for simulations in any other of the (conventional) statistical ensembles like, e.g., the isothermal–isobaric or the grand-canonical ensemble [11]. However, this conventional way of Monte Carlo sampling is prone to fail in practice in cases where the free energy landscape in phase space is 'rough' with a multitude of local energy minima which are separated by free energy barriers. This scenario is found in systems with co-existing phases at or close to a discontinuous (first-order) phase transition, and in systems with conflicting constraints (frustrations) like, e.g., spin glasses. At low temperatures the system will then get trapped in microconfigurations corresponding to one of the many local free energy minima. As a consequence only a small part of the entire phase space is explored within the finite simulation time, which inevitably produces inaccurate ensemble averages of thermodynamic quantities.

Many methods have been proposed in order to overcome this trapping in local free energy minima, among them simulated annealing [12], a widely used method to drive a system towards its global-minimum state. In recent years so-called generalized ensemble algorithms have been devised, like $1/k$ sampling [13], simulated tempering [14,15], entropic sampling [16] and multicanonical sampling [17–19], which all attempt to explore larger parts of the phase space than conventional Monte Carlo sampling and thereby allow the calculation of reliable ensemble averages.

Multicanonical sampling in particular has been recognized as a powerful technique, where one attempts to sample microconfigurations with a uniform (constant) equilibrium probability distribution of energy

$$\mathcal{P}_{\mathrm{mucan}}(E, T) \propto \Omega(E)\rho_{\mathrm{mucan}}(E, T) \overset{!}{=} \mathrm{const}. \tag{3}$$

This can be achieved by choosing non-conventional or 'non-Boltzmann' statistical weights given by

$$\rho_{\mathrm{mucan}}(E, T) \propto \Omega^{-1}(E) = \mathrm{e}^{-S(E)/k_{\mathrm{B}}}, \tag{4}$$

where $S(E) = k_{\mathrm{B}} \ln \Omega(E)$ is the microcanonical entropy. Because of the uniform energy probability distribution a multicanonical simulation corresponds to a random walk in one-dimensional energy space, which is not affected by free energy barriers and therefore allows the system to escape from any local free energy minimum [17–26]. The only problem here is the determination of the multicanonical weights (Eq. (4)), which are not known a priori. Clearly an explicit knowledge of either the density-of-states $\Omega(E)$ or the microcanonical entropy $S(E)$ corresponds to the solution of the statistical mechanics problem of the system under consideration. Since this solution is not known beforehand, the estimators for the multicanonical weights have to be determined in an iterative way in a first step of a multicanonical simulation. Algorithmic aspects including the efficient determination of the multicanonical weights are discussed, e.g., in Refs. [24–26]. For general reviews of the method see Refs. [21–23,27].

Multicanonical sampling has been successfully applied to a wide range of systems undergoing first-order phase transitions. The interfacial tension between co-existing phases was studied for the 2D and 3D Ising model [27,28], for both the 7-state [29–31] and the 10-state [18,32–34] Potts model in 2D, and for liquid–vapor [35,36] and solid–solid [37,38] phase co-existence in model systems. The confinement/deconfinement phase transition in SU(3) gauge theory [39–41] was simulated with the multicanonical technique as well as the electroweak phase transition [42–44]. Applications of the method to systems with conflicting constraints include model systems for spin glasses [45–52], conformational studies of peptides [53–60], studies of the helix–coil transition and of protein folding [61–69], and – in combination with

simulated annealing – hard optimization problems [70].

Variants of the multicanonical method have also been developed. In the so-called 'multimagnetical' variant [27,28,71,72] the rôle of temperature is exchanged for that of a (magnetic) field which drives the phase transition. A combination with cluster updates was termed 'multibondic' [31,73,74], and a combination with multigrid methods has also been developed [75–77]. The 'entropic sampling' technique was proven to be an equivalent formulation of multicanonical sampling [78]. Finally it was shown that the multicanonical approach is not limited to Monte Carlo simulations, but can as well be successfully implemented in Molecular Dynamics simulations, Langevin simulations, and hybrid Monte Carlo simulations [79].

A common denominator of multicanonical sampling and its variants (which in principle have their roots in the 'umbrella sampling' technique developed by Torrie and Valleau in the 1970s [121–123]) is that they are essentially *non-Boltzmann* sampling methods, where non-Boltzmann-type Monte Carlo transition probabilities are employed which have to be determined in an iterative way during the course of the simulation. This additional iterative element is maybe the reason why the multicanonical method – despite its efficiency – has not yet become the common 'workhorse' in Monte Carlo simulation studies, and although numerous successful applications have been reported, it is still a tool used by relatively few experts in the field.

We are convinced that the multicanonical approach deserves the attention of a broader audience, and it is for that purpose that we present in this paper another – equivalent – variant of the multicanonical approach, which we have termed 'shape function method'. It formulates the underlying principle of the multicanonical approach in yet another – and as we believe, particularly transparent – way, which is based on the notion of an 'effective' Hamiltonian (see also Ref. [23]). Our variant attempts efficient sampling of probability distribution functions for systems undergoing first-order phase transitions by adding a suitably chosen *shape function* to the model Hamiltonian. In that way a new effective Hamiltonian is defined.

Boltzmann ('canonical') sampling of this effective Hamiltonian can be shown to be equivalent to non-Boltzmann ('multicanonical') sampling of the original model Hamiltonian. Starting with small system sizes, the shape function (and thereby also the effective Hamiltonian) is then iteratively improved in a series of simulation runs. This includes repeated extrapolations to and subsequent refinements for bigger system sizes, and reweighting of the sampled probability distribution functions to keep track of the system-size dependent transition temperature. The method is, as we will demonstrate, simple and straightforward in its practical implementation, and offers the potential of an easy adaption to more complex model systems.

Since we hope that the present study might contribute to stimulate a more widespread use of the multicanonical approach in future simulation studies, this paper is written with a didactical attitude, and it includes for the sake of completeness a discussion of concepts like distribution functions (histograms), spectral free energies, and the use of shape functions in some detail.

The outline of the paper is as follows. We first introduce equilibrium probability distributions (histograms) and the associated spectral free energy distributions, and show how they are related to thermodynamic free energies relevant for the system under consideration. The reweighting of histograms and spectral free energy distributions is reviewed, and the theoretical predictions for the finite-size scaling behavior of (spectral) free energy barriers between co-existing phases in the case of asymmetric first-order phase transitions are discussed. We then show how in principle efficient (Boltzmann) sampling can be achieved by adding a shape function to the Hamiltonian, and how our approach is related to the entropic and multicanonical sampling techniques. Different ways of implementation of the iterative determination of the optimum shape function are illustrated by applying the method to a lattice model for a membrane consisting of a binary lipid mixture, and to a two-dimensional crystal model which exhibits interfacial melting. These two examples are chosen since they involve strongly first-order transitions and are therefore notoriously difficult to study by conventional Boltzmann sampling

algorithms. The summary includes a discussion of points which should be observed in cases where the method is applied to two- or higher-dimensional histograms.

2. Histograms and spectral free energies

We first introduce histograms and the corresponding 'spectral' free energy functions (cf., e.g., [80]). In order to provide a proper basis for the following discussions, some effort is made in the first part of this section to provide a proper explanation of these entities. The general concepts will be highlighted by using two examples, volume histograms for a simple fluid system in the NpT ensemble, and energy histograms for an arbitrary system. In all examples only the configurational part of the Hamiltonian will be considered, since the particle momenta can be integrated out in the complete partition function [81]. We will also restrict the discussion to one-dimensional histograms. Some comments on the higher-dimensional case will be given at the end of the paper. After the introduction of histograms and spectral free energies we briefly review the reweighting technique introduced by Ferrenberg and Swendsen [82,83] which is an integral part in virtually every iterative method to overcome free energy barriers. We conclude the section on histograms and spectral free energies by discussing the approximative functional form of energy histograms and corresponding spectral free energies for the case of asymmetric first-order phase transitions. We will also briefly review the Lee–Kosterlitz scaling method [84], which in combination with Ferrenberg–Swendsen reweighting allows the determination of the nature (continuous/discontinuous) of a phase transition under consideration, and in the case of discontinuous transitions also allows the determination of the interfacial tension between the coexisting phases.

2.1. Introduction of histograms and spectral free energies

As a first example we consider a simple fluid system. Although the case studies which will be discussed in Section 4 employ lattice models of fixed volume, the example of a fluid system with fluctuating volume is chosen here to demonstrate the general applicability of the technique to be presented here. Before we turn to a system of fluctuating volume, however, it is useful to consider a fluid of fixed volume V first. The internal energy of a microstate is given by $\mathscr{U}(x, V)$, where x denotes the set of particle coordinates. It is useful to consider first the *canonical* ensemble, which is characterized by fixed particle number N, fixed volume V, and fixed temperature T (NVT ensemble).

The canonical partition function is given by [11]

$$Q_\beta(V) = \int \mathscr{D}x \, \mathrm{e}^{-\beta \mathscr{U}(x,V)}, \tag{5}$$

where $\beta = 1/k_\mathrm{B}T$ denotes the inverse temperature (k_B is the Boltzmann constant). The symbolic integration $\int \mathscr{D}x$ is over the whole canonical phase space, i.e., over all particle coordinates x. Here and in the following, fixed intensive variables (like the inverse temperature β) will be noted as subscripts.

The Helmholtz free energy of the fluid is then given by [11]

$$\beta \, F_\beta(V) = -\ln Q_\beta(V). \tag{6}$$

We now make the transition to the NpT or (isothermal–)isobaric ensemble, with fixed pressure p. The volume $\mathscr{V}$ of the fluid is not fixed anymore but fluctuates around its equilibrium value. Note that physical quantities defined for a single microstate (like $\mathscr{U}$ or $\mathscr{V}$) will be denoted by calligraphic capitals, and the corresponding thermal ensemble averages ($U \equiv \langle \mathscr{U} \rangle$, $V \equiv \langle \mathscr{V} \rangle$) by italic roman capitals. Instead of the internal energy $\mathscr{U}(x, V)$ we now use the isobaric Hamiltonian (whose thermal average is the enthalpy of the fluid), which is given by

$$\mathscr{H}_p(x, \mathscr{V}) := \mathscr{U}(x, \mathscr{V}) + p\mathscr{V} \tag{7}$$

and differs from the internal energy by the additive mechanical work term $p\mathscr{V}$ [11]. As the notation indicates, an isobaric microconfiguration is characterized by the set of particle co-ordinates x together with the system volume $\mathscr{V}$. Note that the pressure p as fixed intensive variable is written as a subscript.

The isobaric partition function can be written as a Laplace transform of the canonical partition function [11]

$$Z_{\beta,p} = \int d\mathcal{V} \int \mathcal{D}x \ e^{-\beta\mathcal{H}_p(x,\mathcal{V})}$$

$$= \int d\mathcal{V} Q_\beta(\mathcal{V}) e^{-\beta p\mathcal{V}}, \tag{8}$$

and the thermodynamic potential of the isobaric ensemble is the Gibbs free energy

$$\beta G_{\beta,p} = -\ln Z_{\beta,p}. \tag{9}$$

The normalized probability density (statistical weight) of an isobaric microstate $(x, \mathcal{V})$ at fixed pressure and inverse temperature β is then given by

$$\rho_{\beta,p}(x, \mathcal{V}) = Z_{\beta,p}^{-1} \ e^{-\beta\mathcal{H}_p(x,\mathcal{V})}. \tag{10}$$

We are now ready to introduce the *volume histogram*, which is defined as the (normalized) probability density to find the fluid system at a certain volume V in thermal equilibrium at fixed temperature and pressure (cf. [80]), and is given by

$$\mathcal{P}_{\beta,p}(V) := \int d\mathcal{V} \int \mathcal{D}x \ \delta(V - \mathcal{V})\rho_{\beta,p}(x, \mathcal{V})$$

$$\equiv \langle \delta(V - \mathcal{V}) \rangle_{\beta,p}. \tag{11}$$

It can formally be written as an isobaric ensemble average of the delta function $\delta(V - \mathcal{V})$ [85].

As a probability density, the volume histogram is positive and normalized, as can easily be deduced from its definition:

$$\mathcal{P}_{\beta,p}(V) \geqslant 0 \quad \text{and} \quad \int dV \mathcal{P}_{\beta,p}(V) = 1. \tag{12}$$

In a Monte Carlo simulation (like in principle in any experiment) only discrete microconfigurations and therefore also discrete volume values are sampled. The 'experimental' approximation to the volume histogram defined above is then the distribution of the relative frequencies by which a certain volume value occurs during the simulation. In practice the volume values are often (although not always, cf. Section 4.2) binned in a histogram with bin width ΔV. Assume that in a Monte Carlo simulation of an already equilibrated fluid sample the number of occurrences of microconfigurations in a bin characterized by the (average) volume

value V_i is given by $N_{\beta,p}(V_i)$. The normalized volume histogram is then approximated by

$$\mathcal{P}_{\beta,p}(V_i) \simeq \frac{N_{\beta,p}(V_i)}{\Delta V \sum_j N_{\beta,p}(V_j)}, \tag{13}$$

where the sum in the denominator of the r.h.s. is over all bins and equals the total number of microconfigurations used for the evaluation of the histogram.

What is such a volume histogram good for? First, it allows the calculation of thermal averages (at constant temperature and pressure) of any function $f(\mathcal{V})$ of the volume 'operator' $\mathcal{V}$ by replacing the integration over the isobaric phase space by a simple integration over the volume alone with the volume histogram as weight function. By utilizing the expression $f(\mathcal{V}) = \int dV \ f(V)\delta(V - \mathcal{V})$, we see that

$$\langle f(\mathcal{V}) \rangle_{\beta,p} = \int d\mathcal{V} \int \mathcal{D}x \ f(\mathcal{V})\rho_{\beta,p}(x, \mathcal{V})$$

$$= \int dV \ f(V) \int d\mathcal{V}$$

$$\times \int \mathcal{D}x \ \delta(V - \mathcal{V}) \ \rho_{\beta,p}(x, \mathcal{V})$$

$$= \int dV \ f(V) \ \mathcal{P}_{\beta,p}(V) \tag{14}$$

$$\simeq \Delta V \sum_i f(V_i) \ \mathcal{P}_{\beta,p}(V_i), \tag{15}$$

where the 'experimental' approximation is given in the last line.

This allows, as an example, the calculation of $\langle \mathcal{V} \rangle_{\beta,p}$ and $\langle \mathcal{V}^2 \rangle_{\beta,p}$ and thus of the isothermal compressibility $\kappa_T = \beta(\langle \mathcal{V}^2 \rangle_{\beta,p} - \langle \mathcal{V} \rangle_{\beta,p}^2)/\langle \mathcal{V} \rangle_{\beta,p}$ via the corresponding fluctuation-response formula. The knowledge of the volume histogram $\mathcal{P}_{\beta,p}$ alone does, of course, not allow the calculation of any quantity which cannot be expressed as a function of the volume operator, like, e.g., enthalpy $\langle \mathcal{H}_p \rangle$ or specific heat at constant volume $C_V = (\langle \mathcal{H}_p^2 \rangle - \langle \mathcal{H}_p \rangle^2)/k_B T^2$ [11]. For this purpose either a separate one-dimensional *energy histogram* $\mathcal{P}_{\beta,p}(E)$ (which we will consider as a second example below) or a two-dimensional histogram (joint probability density) of both volume and energy has to be used.

A second, and even more important, reason for the usefulness of the volume histogram is – as we will see in a moment – that it is related to a free energy-like quantity, which in turn is directly related to the Helmholtz free energy of the fluid system. Moreover, the fact that the histogram for a given value of pressure or/and temperature allows the direct evaluation of the corresponding histogram for a different, close-by pressure or/and temperature value via a reweighting technique (see Section 2.2), opens up the possibility for direct determination of the transition temperature for first-order phase transitions.

It follows directly from the definition of the volume histogram that it can be written as an exponential in the following way:

$$\mathscr{P}_{\beta,p}(V) = \frac{1}{Z_{\beta,p}} \int d\mathscr{V} \, \delta(V - \mathscr{V}) Q_\beta(\mathscr{V}) \, e^{-\beta p \mathscr{V}}$$
$$= \frac{Q_\beta(V)}{Z_{\beta,p}} e^{-\beta p V}$$
$$= e^{-\beta \left[F_\beta(V) + pV - G_{\beta,p} \right]}. \tag{16}$$

This now suggests to rewrite also the lhs as an exponential by defining in analogy with the Helmholtz or Gibbs free energies the so-called *spectral free energy* corresponding to the volume histogram (cf., e.g., [80]) by

$$\beta \mathscr{F}_{\beta,p}(V) := -\ln \mathscr{P}_{\beta,p}(V). \tag{17}$$

Here the adjective 'spectral' refers to the fact that this quantity is related to a distribution function ($\mathscr{P}_{\beta,p}(V)$) which was obtained by adding up only contributions from a certain subset of microstates of the isobaric phase space corresponding to a given value of the system volume V.

With this definition, we obtain immediately a relation between the spectral free energy and the Helmholtz and the Gibbs free energies:

$$\mathscr{F}_{\beta,p}(V) = F_\beta(V) + pV - G_{\beta,p}, \tag{18}$$

which explains why $\mathscr{F}_{\beta,p}(V)$ is termed a 'free energy'.

There are a few comments to be made on the last equation: First, we see that in this example the spectral free energy is – unlike the thermodynamic free energies $F_\beta(V)$ and $G_{\beta,p}$ – a function of three

instead of only two variables. However, in the *isothermal–isobaric* ensemble chosen here two of these variables (β and p) are considered to be kept fixed, while only the third variable (V) is varying (fluctuating). In this sense, and apart from the trivial term pV and the 'normalization constant' $G_{\beta,p}$ ('constant' in the sense that both β and p are fixed), the spectral free energy $\mathscr{F}_{\beta,p}(V)$ essentially reflects the functional form of the *Helmholtz* free energy $F_\beta(V)$. The latter, however, is the free energy which characterizes the *canonical* ensemble with fixed temperature and volume. The statistics of the volume fluctuations thus allows – at least in principle, and up to a constant – the determination of the free energy corresponding to the ensemble with fixed volume.

Second, Eq. (18) resembles – apart from the (irrelevant) 'constant' $G_{\beta,p}$ – the Landau free energy function for a simple fluid with intensive control parameters β and p, if $F_\beta(V)$ is replaced by a free energy ansatz in terms of powers of the relevant order parameter (the density difference between the gas and the liquid state in this case). This implies that the graph of $\mathscr{F}_{\beta,p}(V)$ is expected to resemble the well-known LANDAU free energy function (e.g., with a double-minimum structure close to a phase transition point, as will be discussed in Section 2.3). It should be emphasized, however, that despite this similarity the spectral free energy as defined in Eq. (17) is a quantity which does not rely on any mean-field-type approximative schemes.

We now turn to a second example in order to highlight the concepts of histograms and spectral free energies, and consider an arbitrary (classical) system in an ensemble we do not wish to specify further, but in which the system may be described by an effective 'ensemble Hamiltonian' $\mathscr{H}(x)$. Here x denotes collectively the set of all microscopic degrees of freedom (particle coordinates, spin variables, etc.) as well as additional physical quantities (like the volume in the case of the isobaric ensemble) which together with the microscopic co-ordinates label the microstates of the ensemble in a unique way. We are now interested in the energy fluctuations at fixed temperature, which in analogy with the volume histogram are described by an energy histogram.

The partition function of the system is given by

$$Z_\beta = \int \mathscr{D}x \, \mathrm{e}^{-\beta \mathscr{H}(x)}, \qquad (19)$$

and the free energy by

$$\beta F_\beta = -\ln Z_\beta. \qquad (20)$$

The energy histogram is now defined in analogy with the volume histogram by

$$\mathscr{P}_\beta(E) := \langle \delta[E - \mathscr{H}(x)] \rangle_\beta$$
$$= \frac{1}{Z_\beta} \int \mathscr{D}x \, \delta[E - \mathscr{H}(x)] \, \mathrm{e}^{-\beta \mathscr{H}(x)}. \qquad (21)$$

Because of the delta function, this expression can be further simplified by replacing $\mathscr{H}(x)$ in the exponential of the rhs by E with the result

$$\mathscr{P}_\beta(E) = \frac{\mathrm{e}^{-\beta E}}{Z_\beta} \int \mathscr{D}x \, \delta[E - \mathscr{H}(x)]. \qquad (22)$$

Now

$$\int \mathscr{D}x \, \delta[E - \mathscr{H}(x)] =: \Omega(E) = \mathrm{e}^{S(E)/k_\mathrm{B}} \qquad (23)$$

is simply the density of states at energy E and can be written in terms of the entropy $S(E)$ [86]. By expressing the partition function in the denominator of Eq. (22) by the free energy F_β, also the energy histogram can be re-written as an exponential:

$$\mathscr{P}_\beta(E) = \mathrm{e}^{-\left[\beta E - S(E)/k_\beta - \beta F_\beta\right]}. \qquad (24)$$

This suggests the definition of an energy-dependent spectral free energy by

$$\beta \mathscr{F}_\beta(E) := -\ln \mathscr{P}_\beta(E). \qquad (25)$$

From Eqs. (24) and (25) we then obtain the relation

$$\beta \mathscr{F}_\beta(E) = -S(E)/k_\mathrm{B} + \beta E - \beta F_\beta, \qquad (26)$$

i.e., $\beta \mathscr{F}_\beta(E)$ is (apart from the trivial linear term βE and the 'constant' βF_β) essentially given by the entropy $S(E)$.

After these two examples it should be clear how the definition of histograms and related spectral free energies can be generalized to other cases, as well as to two- or even higher-dimensional cases (histograms and spectral free energies with two or more independent variables).

2.2. Histogram reweighting

In this section we briefly review the basic facts about the 'histogram reweighting' technique which has been introduced into Monte Carlo simulation methodology by Ferrenberg and Swendsen [82,83]. Since then it has evolved into a powerful method for extracting as much significant information from histograms sampled in simulations as possible. As an example we discuss in the following the reweighting of energy histograms and the associated spectral free energy as introduced in the previous section (Eqs. (24) and (25)) with respect to temperature.

Ferrenberg and Swendsen noticed that from an energy histogram $\mathscr{P}_{\beta_0}(E)$ sampled at a given inverse temperature β_0, a corresponding histogram $\mathscr{P}_\beta(E)$ for any inverse temperature value β *sufficiently close* to β_0 can be evaluated simply by reweighting the original histogram. From Eq. (23) we see that the density of states $\Omega(E)$ does not depend on temperature. By employing Eq. (22) we can write

$$Z_\beta \, \mathrm{e}^{\beta E} \mathscr{P}_\beta(E) = \Omega(E) = Z_{\beta_0} \, \mathrm{e}^{\beta_0 E} \mathscr{P}_{\beta_0}(E). \qquad (27)$$

The two energy histograms at inverse temperatures β_0 and β are therefore related by

$$\mathscr{P}_\beta(E) = \frac{Z_{\beta_0}}{Z_\beta} \mathscr{P}_{\beta_0}(E) \, \mathrm{e}^{-(\beta - \beta_0)E}. \qquad (28)$$

Since the histograms $\mathscr{P}_{\beta_0}(E)$ and $\mathscr{P}_\beta(E)$ are by definition normalized, the prefactor Z_{β_0}/Z_β clearly is a normalization factor and thus has to be given by $\left[\int \mathrm{d}E' \, \mathrm{e}^{-(\beta - \beta_0)E'} \, \mathscr{P}_{\beta_0}(E')\right]^{-1}$. In a more formal way this can also be seen from the following transformation of Z_{β_0}/Z_β:

$$\left(\frac{Z_{\beta_0}}{Z_\beta}\right)^{-1} = \frac{1}{Z_{\beta_0}} \int \mathscr{D}x \, \mathrm{e}^{-\beta \mathscr{H}(x)}$$
$$= \frac{1}{Z_{\beta_0}} \int \mathscr{D}x \, \mathrm{e}^{-(\beta - \beta_0)\mathscr{H}(x)} \mathrm{e}^{-\beta_0 \mathscr{H}(x)}$$
$$= \left\langle \mathrm{e}^{-(\beta - \beta_0)\mathscr{H}} \right\rangle_{\beta_0}$$
$$= \int \mathrm{d}E' \, \mathrm{e}^{-(\beta - \beta_0)E'} \, \mathscr{P}_{\beta_0}(E'), \qquad (29)$$

where the $\langle \cdots \rangle_{\beta_0}$ denotes an ensemble average at inverse temperature β_0.

The final reweighting formula for energy histograms is thus given by

$$\mathscr{P}_\beta(E) = \frac{\mathscr{P}_{\beta_0}(E)\,\mathrm{e}^{-(\beta-\beta_0)E}}{\int \mathrm{d}E'\,\mathscr{P}_{\beta_0}(E')\,\mathrm{e}^{-(\beta-\beta_0)E'}}, \qquad (30)$$

or for a histogram sampled by Monte Carlo simulation by

$$\mathscr{P}_\beta(E_i) \simeq \frac{\mathscr{P}_{\beta_0}(E_i)\,\mathrm{e}^{-(\beta-\beta_0)E_i}}{\Delta E \sum_j \mathscr{P}_{\beta_0}(E_j)\,\mathrm{e}^{-(\beta-\beta_0)E_j}}. \qquad (31)$$

For the corresponding spectral free energies $\mathscr{F}_{\beta_0}(E)$ and $\mathscr{F}_\beta(E)$ the reweighting formula has the particularly simple form

$$\beta\mathscr{F}_\beta(E) = \beta_0\mathscr{F}_{\beta_0}(E) + (\beta-\beta_0)E + K_{\beta,\beta_0}, \qquad (32)$$

where K_{β,β_0} is the logarithm of the normalization prefactor derived in Eq. (29) which does not depend on energy but only on the two temperatures under consideration. Up to the 'constant' K_{β,β_0} we can therefore construct the graph of $\beta\mathscr{F}_\beta(E)$ from the graph of the original spectral free energy $\beta_0\mathscr{F}_{\beta_0}(E)$ by adding point-wise the linear function $(\beta-\beta_0)E$.

As already mentioned, reweighting *in practice* only works well for temperatures T sufficiently close to the original temperature T_0. The reason for this is easily understood if we consider as an example an elevated temperature T_0, where the system is in a single (disordered) phase. The energy histogram $\mathscr{P}_{\beta_0}(E)$ then exhibits a single peak centered at a certain energy value E_0^*. By reweighting the initial histogram to, say, a temperature $T > T_0$, the 'low-energy' tail of $\mathscr{P}_{\beta_0}(E)$ is suppressed by the factor $\mathrm{e}^{-(\beta-\beta_0)E}$ while the 'high-energy' tail is magnified. As a result the reweighed histogram will still exhibit a single peak, but shifted to a slightly higher energy $E^* > E_0^*$. However, with increasing energy $E > E_0^*$ the relative errors of the bins of the original histogram become also increasingly higher. Magnifying those bin values during the reweighting process results in a loss of statistical accuracy for the bins where the peak is located after the reweighting. This prevents the evaluation of significant histogram data for temperatures T not sufficiently close to T_0.

In any case a thorough analysis of error propagation of the reweighted data is necessary, and

becomes indispensable when – as a further development of the 'single-histogram' reweighting technique – several individual histograms (sampled at different temperature values) are combined in order to construct a histogram for a broader range of temperature values ('multi-histogram' reweighting). We do not here discuss this and other sophisticated variants of histogram reweighting and the corresponding error analysis but instead refer to a review article devoted to this subject [87]. The application of the single-histogram method as outlined in this section to reweighting with respect to variables other than temperature is straightforward, as well as the generalization to the reweighting of two-dimensional histograms.

In the next section we will discuss the application of reweighting to energy histograms sampled in the vicinity of an asymmetric first-order phase transition.

2.3. Asymmetric first-order phase transitions

So far only general properties of histograms and spectral free energies have been discussed. We now focus on the properties of these entities for systems in the neighborhood of a first-order transition. (For a general review of first-order phase transitions see, e.g., [88]). More specifically, we consider here the case of a temperature-driven 'asymmetric' first-order transitions (like the solid–liquid transition), where the two coexisting phases (ordered and disordered in the case of the melting transition) cannot be related by symmetry operations [89]). In the following we review the theoretical predictions for the functional form of histograms and spectral free energies and their dependence on the system size L [80,90–94].

As an example, we consider here histograms of energy fluctuations at fixed temperature. We start with a qualitative description of the energy histogram: At fixed linear system size L and at temperatures well *below* the transition temperature $T_t(L)$ [95], the histogram exhibits only a single peak corresponding to the ordered phase. At temperatures well *above* $T_t(L)$, a single peak at elevated energies (when compared to the peak of the ordered phase) represents the disordered phase. At

temperatures in the neighborhood (below as well as above) of $T_t(L)$ both peaks are present, although with different amplitudes (heights) depending on temperature: When the temperature is increased across $T_t(L)$, the amplitude of the 'ordered peak' decreases, while the amplitude of the 'disordered peak' increases. Also the peak *positions* shift slowly when the temperature is varied [96]. At a fixed temperature the peak positions shift also as a function of the system size L, and the peak widths (which represent the temperature interval over which the transition is 'smeared out' in finite systems) decrease with increasing L, when the histogram is plotted as function of the energy *density*, i.e., energy per volume, E/L^d. For very small system sizes the two peaks may even become so broad that they overlap considerably, and the histogram then exhibits a broad double-peak structure close to $T_t(L)$.

The two peaks of the energy histogram correspond to two minima of the associated spectral free energy. The drastically reduced probability density between the two histogram peaks corresponds to a spectral free energy barrier which has to be overcome when the system is driven from one phase to the other by equilibrium fluctuations.

After this outline of the qualitative behavior, we now discuss matters in a more quantitative way, and show that the two peaks of the histogram can to a good approximation be represented by Gaussians. Within this approximation, we will present the functional form of the energy histogram at $T_t(L)$ for fixed system size L. (To avoid a clumsy notation, in the following the explicit notation of L in the formulas will be suppressed.)

We first consider the spectral free energy $\mathscr{F}_{\beta_t}(E)$ corresponding to the the energy histogram at the transition temperature T_t, and calculate its first and second partial derivatives with respect to E. From Eq. (26) we know

$$\beta_t \mathscr{F}_{\beta_t}(E) = \beta_t E - S(E)/k_B - \beta_t F_{\beta_t}. \tag{33}$$

The first partial derivative of Eq. (33) is directly related to the equation of state $\beta(E) = k_B^{-1} \partial S(E)/\partial E$ (e.g., [80]):

$$\frac{\partial}{\partial E}\left[\beta_t \mathscr{F}_{\beta_t}(E)\right] = \beta_t - \beta(E), \tag{34}$$

while the second partial derivative is related to the specific heat at constant volume (the index 'V' is omitted here) $C(E) = \partial E/\partial T = -k_B \beta(E)^2[\partial \beta(E)/\partial E]^{-1}$ [80]:

$$\frac{\partial^2}{\partial E^2}\left[\beta_t \mathscr{F}_{\beta_t}(E)\right] = \frac{k_B}{C(E)}\beta(E)^2. \tag{35}$$

Let E_t^- and E_t^+ denote the energy values of, respectively, the 'ordered' and the 'disordered' histogram peak at the transition temperature $T_t(L)$, and $C_t^{\pm} \equiv C(E_t^{\pm})$ the limits of the specific heat for $T \to T_t \pm 0$. We now expand the spectral free energy at $T_t(L)$ separately around its minima at $E = E_t^{\pm}$ to second order in E. Since $\beta(E_t^{\pm}) = \beta_t$, the terms linear in $E - E_t^{\pm}$ vanish, and we get the two truncated expansions (as distinguished by the superscripts '$\pm$')

$$\beta_t \mathscr{F}_{\beta_t}(E) \approx \beta_t \mathscr{F}_{\beta_t}(E_t^{\pm}) + \frac{\left(\beta_t E - \beta_t E_t^{\pm}\right)^2}{2C^{\pm}/k_B}. \tag{36}$$

The constants $\beta_t \mathscr{F}_{\beta_t}(E_t^{\pm})$ in these approximations can be rewritten in a way which takes the finite system size more directly into account: First, we have $\beta_t \mathscr{F}_{\beta_t}(E_t^{\pm}) = \beta_t E_t^{\pm} - S(E_t^{\pm})/k_B - \beta_t F_{\beta_t}$ according to Eq. (33). Second, it can be shown that for a *finite* system size L the relation between the Helmholtz free energy in the *canonical* ensemble and the *microcanonical* entropy is (for an arbitrary inverse temperature β) given by $\beta F_\beta \approx \beta E - S(E)/k_B - \ln \sqrt{2\pi C(E)/k_B \beta^2}$, where the last term containing the specific heat $C(E)$ is a finite-size correction term of the order of $\ln L$. Evaluating the latter equation for $\beta = \beta_t$ (and $E = E_t^{\pm}$) and inserting it into the former, we get the result

$$\beta_t \mathscr{F}_{\beta_t}(E_t^{\pm}) \approx -\ln \sqrt{\frac{k_B \beta_t^2}{2\pi C^{\pm}}}. \tag{37}$$

In a final step the energy histogram $\mathscr{P}_{\beta_t}(E)$ is now approximated by the superposition of two Gaussian peaks, centered at E_t^- and E_t^+, whereby each of these two Gaussians results from exponentiating the *negative* quadratic approximations of $\beta_t \mathscr{F}_{\beta_t}(E)$ in the neighborhood of the respective minimum:

$$\mathscr{P}_{\beta_t}(E) \propto \sqrt{\frac{k_B \beta_t^2}{2\pi C^-}} \exp\left[-\frac{(\beta_t E - \beta_t E_t^-)^2}{2C^-/k_B}\right]$$

$$+ \sqrt{\frac{k_B \beta_t^2}{2\pi C^+}} \exp\left[-\frac{(\beta_t E - \beta_t E_t^+)^2}{2C^+/k_B}\right]. \quad (38)$$

We now briefly discuss the properties of the energy histogram *at the transition temperature*. First, the *distance* between the two peaks scales in a trivial way with the system volume, i.e., $E_t^+ - E_t^- \propto L^d$. For that reason a plot of the histogram as a function of the energy *density* E/L^d is suitable when comparing histograms and spectral free energy curves for different system sizes L. Second, we see that the two peaks do in general not have the same *widths*, which are proportional to $\sqrt{C^\pm} \propto L^{d/2}$. (Note, however, that the peak widths are proportional to $\sqrt{C^\pm}/L^d \propto L^{-d/2}$, when plotted as a function of the energy density). Third, the *heights* (amplitudes) are also different, and proportional to $1/\sqrt{C^\pm} \propto L^{-d/2}$.

Thus *at the transition temperature* $T_t(L)$ the areas underneath the two peaks (the '*weights*' of the peaks), which are proportional to the products of their respective widths and heights, are the same [91–93]. Since these areas are simply the probabilities to find the system in the ordered or the disordered phase, respectively, we see that this characterization of the transition temperature corresponds to an 'equal-likelihood' criterion for phase coexistence. At $T_t(L)$ the system is with equal probability found in either of the two competing phases. With increasing L, however, the criterion of equal peak weights for phase co-existence becomes asymptotically equivalent to the criterion of equal peak heights, which was originally derived on the basis of Landau theory-type arguments. Practical considerations concerning the localization of $T_t(L)$ will be discussed in Section 3.3. One should bear in mind, that the equal-weight criterion was derived here for the case of a *non-degenerate* ordered phase. At the end of this subsection we will discuss whether these conclusions have to be modified for the case of an *n*-fold *degenerate* ordered phase.

We now keep the system size L fixed, but vary the temperature in the neighborhood of $T_t(L)$, i.e.,

$T_t \to T = T_t + \delta T$, or equivalently $\beta_t \to \beta = \beta_t + \delta\beta$ ($\delta\beta < 0$ if $\delta T > 0$). To a first approximation, the modification of the histogram can be described by the reweighting formula (cf., Eq. (30))

$$\mathscr{P}_\beta(E) \propto \mathscr{P}_{\beta_t}(E) e^{-(\beta-\beta_t)E}. \quad (39)$$

This has the following effects: The peak *positions* shift in a first approximation according to the equation of state, i.e., $E_t^\pm \to E^\pm \approx E_t^\pm + (\partial E_t^\pm/\partial T)\delta T = E_t^\pm + C^\pm \delta T$. The *height* of the 'ordered peak' is in good approximation scaled by the factor $\exp(-\delta\beta E_t^-)$, while the height of the 'disordered peak' is scaled by $\exp(-\delta\beta E_t^+)$. In contrast, changes of the peak *widths* upon temperature variation are almost negligible.

For the Gaussian double-peak approximation, as given by Eq. (38), the specific heat as a function of energy can be calculated and the position of the maximum (which determines $T_t(L)$) be evaluated. It turns out that the deviation of the finite system transition temperature from the infinite system transition temperature scales with the system volume [91,92,94]:

$$T_t(L) - T_t(\infty) \propto L^{-d}. \quad (40)$$

Therefore in a *finite-size scaling plot* of $T_t(L)$ vs. L^{-d}, asymptotically (for $L^{-d} \to 0$) an affine-linear relation should be observed from which $T_t(\infty)$ can be determined by extrapolation to $L^{-d} = 0$.

According to Eq. (38) the (spectral) free energy barrier between the ordered and the disordered phase should approximately scale with the system size L^d. However, the derivation of Eq. (38) was entirely based on expansions around the the minima of $\mathscr{F}_{\beta_t}(E)$ corresponding to the two coexisting phases. The existence of so-called 'connecting states' at energies in between E_t^- and E_t^+, i.e., of microconfigurations in which domains of both phases are present, was not taken into account. The typical 'connecting state' exhibits an ordered and a disordered domain. They are typically separated by one or at most two rather flat interfaces, depending on the employed boundary conditions: While for free boundary conditions a single interface with $(d-1)$-dimensional 'area' $\propto L^{d-1}$ should be expected, periodic boundary conditions on the other hand often lead to *two* such interfaces.

From these arguments it is easily seen that the leading contribution to the (spectral) free energy barrier between the two competing phases *at the transition temperature* $T_t(L)$ does not scale as L^d, but as L^{d-1}

$$\Delta\mathcal{F}_{\beta_t} \approx r\gamma_t L^{d-1} + \mathcal{O}(L^{d-2}), \tag{41}$$

where r is the number of interfaces present in the system, and γ_t denotes the interfacial tension (per unit 'area') at the transition temperature. This relation therefore allows the interfacial tension to be obtained from simulation data.

In addition, Eq. (41) it is also the basis of a procedure suggested by Lee and Kosterlitz [84] to identify the nature (first-order vs. second-order) of a phase transition. While for first-order transitions the energy barrier increases with system size according to Eq. (41), it asymptotically approaches a constant value in the case of a continuous phase transition, i.e., at the critical point, since the two phases become indistinguishable in the thermodynamic limit ($\gamma_t \to 0$), and the free energy barrier will therefore not depend on the interfacial 'area' anymore. This method to elucidate the nature of a transition supplements other, equally powerful methods like Binder's forth-order cumulant method (cf., e.g., [90]) and Borgs' method [92].

So far the ordered phase was assumed to be non-degenerate. The generic case, however, is an n-fold degenerate ordered phase, i.e., the ordered phase can exhibit n different 'domain types' of the same symmetry. These different domain types correspond to n different 'pockets' in phase space, but contribute to the same ordered peak in the energy histogram. Formulated in different words: In a n-dimensional probability distribution (histogram) as a function of energy and $n-1$ appropriately chosen linear combinations of order parameter components characterizing the ordered phase, the different ordered domain types would give rise to n peaks, which, when projected onto the energy axis, would superimpose to the single 'ordered peak' of the one-dimensional energy histogram. Together with the single 'disordered peak' there are therefore $n+1$ peaks in the high-dimensional histogram near the phase transition.

During the time evolution of the system in equilibrium at $T_t(L)$, transitions are – at least in principle, i.e., for a sufficiently long observation time – possible between any of the $n+1$ pockets in phase space. The frequency at which these transitions actually occur, however, depends on the height of the respective effective (spectral) free energy barriers between these pockets. In order to see if the criterion for the determination of $T_t(L)$ has to be modified in the case of a degenerate ordered phase, these free energy barriers have to be discussed in more detail.

The free energy barrier between the disordered and the ordered peak in the one-dimensional energy histogram reflects the n free energy barriers between the disordered phase and any of the ordered domain types, respectively. Each of these n free energy barriers in the higher-dimensional histogram can be assumed to have exactly the same shape. Therefore the frequency of direct transitions between the disordered phase and any ordered domain type is the same for all ordered domain types. Note that γ_t in Eq. (41) should now be interpreted as the effective interfacial tension between the disordered phase and *any* type of ordered domain.

Between the n ordered domain types there are $n(n-1)/2$ direct transitions possible. The corresponding $n(n-1)/2$ barriers of the high-dimensional spectral free energy can also be assumed to have exactly the same shape. However, the latter free energy barriers do not show up as a barrier in the one-dimensional spectral free energy, because they are located in a $(n-1)$-dimensional hyperspace which is orthogonal to the energy axis. Nevertheless also for each such free energy barrier a scaling relation analogous to Eq. (41) can be assumed, with γ_t replaced by the *effective* interfacial tension between two different ordered domain types.

For relatively small system sizes, when all free energy barriers are still of moderate size, so that any direct transition between the $n+1$ pockets in phase space occurs with sufficiently high frequency within the given simulation time, the dynamics of the system may be visualized by a symbolic sequence like $\ldots \to D \to O_i \to O_j \to D \to O_k \to D \to O_l \to O_m \to O_n \to D \to \ldots$, where D denotes

the disordered phase, and $O_i, O_j, \ldots$ the ordered domain types.

However, when we now increase the system size, a crucial difference becomes apparent between the free energy barriers between the disordered state and any of the ordered domain types on the one side, and the ones between any pair of ordered domain types on the other side. As we will see in the next section, iterative techniques (like the 'shape function method') can be constructed which are based on the one-dimensional energy histogram and histogram reweighting. These techniques will allow us successively to gain a better knowledge of the free energy barrier between the disordered and the ordered peak. This means in the case of a degenerate ordered phase, that we will be able to implicitly 'flatten' the free energy barriers for direct transitions between the disordered phase and any ordered domain types. The free energy barriers for direct transitions between any pair of ordered domain, however, will only marginally be affected by this procedure. With increasing system size these barriers will increase in size until direct transitions between any pair of ordered domains will be effectively suppressed within a finite simulation time.

The time evolution of the system may then be characterized by a symbolic sequence like $\ldots \to D \to O_i \to D \to O_j \to D \to O_k \to D \to \ldots$. Right at the transition temperature $T_t(L)$, the system can then be observed with probability $1/2$ in the disordered phase and with probability $1/2$ in any of the ordered domains. The system thus behaves as if only a single non-degenerate ordered phase would exist, and the domain type of this ordered phase does not matter.

This means that the '*experimental*' energy histogram which we will be able to obtain for bigger system sizes with, e.g., the shape function method corresponds in fact to Eq. (21) with the summation (integration) over the phase space *essentially limited* to the microstates corresponding to the disordered phase and a *single* ordered domain type and the corresponding 'connecting microstates'. Then Eqs. (38) and (40) do not have to be modified: The equal-weight criterion (or the equal-height criterion for big system sizes) for the ordered and the disordered peak can be applied unchanged.

3. Monte Carlo sampling with shape functions

In this section we introduce shape functions and discuss their effect on histograms and in particular on spectral free energy distributions. Performing Monte Carlo simulations with shape functions can be viewed as a special case of 'non-Boltzmann sampling', and therefore we will briefly discuss the meaning of this term. Shape functions can be employed to 'flatten' spectral free energy barriers associated with first-order phase transition as reviewed in the last section. The general principle how this can be achieved and the resulting iterative scheme are presented, and some details of the implementation of this technique are discussed.

3.1. Introduction of shape functions

Assume the physical system under consideration is described by a model Hamiltonian $\mathscr{H}_1(x)$, the *physical* Hamiltonian. We are interested in sampling the spectral free energy distribution associated with the histogram of a fluctuating physical observable A, such as the energy of the system, or the volume in the case of a fluid in the isothermal-isobaric ensemble (cf. Section 2.1). We now introduce a second Hamiltonian $\mathscr{H}_2(x)$ which depends on exactly the same set of microscopic coordinates x (i.e., the phase space is the same as for $\mathscr{H}_1(x)$), which differs from $\mathscr{H}_1(x)$ only by an arbitrary function of the 'operator' $\mathscr{A}(x)$ associated with the observable A under consideration:

$$\mathscr{H}_2(x) := \mathscr{H}_1(x) + f[\mathscr{A}(x)]. \qquad (42)$$

We term the function $f[\mathscr{A}(x)]$ a *shape function* since it modifies, as we will see below, the shape of the probability distribution of $\mathscr{A}$ and of the associated spectral free energy. We shall refer to the modified Hamiltonian $\mathscr{H}_2(x)$ as the *non-physical* Hamiltonian, since it does generally not correspond to any real physical system. For each of the two Hamiltonians $\mathscr{H}_1(x)$ and $\mathscr{H}_2(x)$ we can now define partition functions and ensemble averages and deduce the relations between corresponding quantities belonging to the two sets. Quantities corresponding to $\mathscr{H}_1(x)$ and $\mathscr{H}_2(x)$ will be distinguished by the indices '1' and '2', respectively.

First, the partition function Z_2 associated with $\mathscr{H}_2$ can be expressed in terms of the partition function Z_1 associated with $\mathscr{H}_1$ and an ensemble average $\langle\ldots\rangle_1$ with respect to $\mathscr{H}_1$:

$$
\begin{aligned}
Z_2 &= \int \mathscr{D}x \ e^{-\beta\mathscr{H}_2(x)} \\
&= Z_1 \ \frac{1}{Z_1} \int \mathscr{D}x \ e^{-\beta f[\mathscr{A}(x)]} e^{-\beta\mathscr{H}_1(x)} \\
&= Z_1 \ \langle e^{-\beta f(\mathscr{A})}\rangle_1.
\end{aligned}
\tag{43}
$$

Second, the ensemble average of an operator $\mathcal{O}(x)$ with respect to the nonphysical Hamiltonian can be expressed in terms of ensemble averages with respect to the physical Hamiltonian

$$
\begin{aligned}
\langle\mathcal{O}\rangle_2 &= \frac{1}{Z_2} \int \mathscr{D}x \ \mathcal{O}(x) e^{-\beta\mathscr{H}_2(x)} \\
&= \frac{Z_1}{Z_2} \frac{1}{Z_1} \int \mathscr{D}x \ \mathcal{O}(x) \ e^{-\beta f[\mathscr{A}(x)]} e^{-\beta\mathscr{H}_1(x)} \\
&= \frac{\langle \mathcal{O} \ e^{-\beta f(\mathscr{A})}\rangle_1}{\langle e^{-\beta f(\mathscr{A})}\rangle_1},
\end{aligned}
\tag{44}
$$

where we have employed Eq. (43) to substitute $\langle e^{-\beta f(\mathscr{A})}\rangle_1$ for $(Z_1/Z_2)^{-1}$. With the special choice $\mathcal{O} \equiv \delta[A - \mathscr{A}(x)]$ the relation between the histograms $\mathscr{P}_2(A)$ and $\mathscr{P}_1(A)$ corresponding to the nonphysical and physical Hamiltonian, respectively, is obtained:

$$
\begin{aligned}
\mathscr{P}_2(A) &= \frac{\langle \delta[A - \mathscr{A}(x)]e^{-\beta f(\mathscr{A})}\rangle_1}{\langle e^{-\beta f(\mathscr{A})}\rangle_1} \\
&= \frac{\langle \delta[A - \mathscr{A}(x)]\rangle_1 \ e^{-\beta f(A)}}{\langle e^{-\beta f(\mathscr{A})}\rangle_1} \\
&= \frac{\mathscr{P}_1(A) \ e^{-\beta f(A)}}{\int \mathrm{d}A' \ \mathscr{P}_1(A') \ e^{-\beta f(A')}}.
\end{aligned}
\tag{45}
$$

For the corresponding spectral free energies we obtain the particularly simple form

$$
\beta\mathscr{F}_2(A) = \beta\mathscr{F}_1(A) + \beta f(A) + K,
\tag{46}
$$

where K is the logarithm of the denominator in the last line of Eq. (45) and does not depend on A but only on the (inverse) temperature. Hence two Hamiltonians which differ by some shape function $f[\mathscr{A}(x)]$ give rise to spectral free energy functions which – apart from the 'constant' K – only differ by the function $f(A)$.

Two remarks seem to be appropriate here. First, one should note the structural similarity between Eqs. (45) and (46) derived in this section, and, respectively, Eqs. (30) and (32) pertinent to the histogram reweighting technique (Section 2.2). The relation between these two pairs of formulas can be easily understood by considering as an example the Hamiltonian $\mathscr{H}_h(x) = \mathscr{U}(x) - h\mathscr{M}(x)$ of a system of spins (denoted collectively by x) with internal energy $\mathscr{U}$, magnetization $\mathscr{M}$, and magnetic field h. The reweighting of a histogram $\mathscr{P}_{h_0}(M)$ of the magnetization, sampled for a specific value h_0 of the magnetic field, to a histogram $\mathscr{P}_h(M)$ for a field value h sufficiently close to the original value h_0, turns out to be mathematically completely equivalent to a formulation in terms of shape functions, when the following identifications are made in Eq. (42): $\mathscr{H}_1 \equiv \mathscr{H}_{h_0}$, $\mathscr{H}_2 \equiv \mathscr{H}_h$, $\mathscr{A} \equiv \mathscr{M}$, and $f(\mathscr{A}) \equiv f(\mathscr{M}) = -(h - h_0)\mathscr{M}$. In this case the 'unphysical' Hamiltonian $\mathscr{H}_2$ describes a real physical situation: the same spin system, but for a different field value h. Note, however, that this mathematical equivalence between the reweighting technique and the shape function approach only holds in cases where the quantity $\mathscr{A}$ is (via a 'coupling constant') additively coupled to the (physical) Hamiltonian under consideration.

The second remark concerns the term *non-Boltzmann* sampling, which is frequently used in this context. It refers to a situation where statistical weights of microconfigurations are used which apparently deviate from the 'normal' Boltzmann-type exponentials associated with the effective Hamiltonian of the equilibrium ensemble under consideration. As a closer inspection reveals, however, this terminology makes only sense if one refers to the Hamiltonian with respect to which a statistical average is calculated. As an example, let us again consider Eq. (44) which expresses the average of an operator $\mathcal{O}(x)$ with respect to Hamiltonian $\mathscr{H}_2(x)$ in terms of averages with respect to Hamiltonian $\mathscr{H}_1(x)$. In the first line the 'Boltzmann factor' $e^{-\beta\mathscr{H}_2(x)}$ appears as a statistical weight in the integral. In the second line, on the other hand, there is the 'Boltzmann factor' $e^{-\beta\mathscr{H}_1(x)}$, but in addition there is also the factor $e^{-\beta f[\mathscr{A}(x)]}$. *Without* the latter, Z_1^{-1} times the integral

could be interpreted as the average of $\mathcal{O}(x)$ *with respect to* $\mathcal{H}_1$. The additional exponential factor $e^{-\beta f[\mathcal{A}(x)]}$ then acts as a 'non-Boltzmann correction'. Likewise, if we consider the corresponding Metropolis transition probability $\pi(x_i \to x_j)$ for a Monte Carlo move from microconfiguration x_i to x_j [97]

$$\pi(x_i \to x_j) = \min\left(1, e^{-\beta\{\mathcal{H}_2(x_j) - \mathcal{H}_2(x_i)\}}\right)$$
$$= \min\left(1, e^{-\beta\{\mathcal{H}_1(x_j) - \mathcal{H}_1(x_i)\} - \beta\{f[\mathcal{A}(x_j)] - f[\mathcal{A}(x_i)]\}}\right) \quad (47)$$

when a simulation is performed with respect to Hamiltonian $\mathcal{H}_2$, then in the second line a 'non-Boltzmann correction' appears in the exponent in addition to the energy difference $\mathcal{H}_1(x_j) - \mathcal{H}_1(x_i)$, evaluated by employing $\mathcal{H}_1$ instead of $\mathcal{H}_2$. From both Eqs. (44) and (47) we see that Boltzmann sampling with respect to $\mathcal{H}_2$ is equivalent to *non-*Boltzmann sampling with respect to $\mathcal{H}_1$. The term non-Boltzmann sampling is specifically employed in situations, where $\mathcal{H}_1$ denotes a 'physical' Hamiltonian and $\mathcal{H}_2$ an associated 'non-physical' Hamiltonian, and where the focus is implicitly on the physical Hamiltonian. This point of view will also be adopted in the following section, where the general simulation scheme for the iterative flattening of (spectral) free energy barriers will be outlined.

3.2. Flattening free energy barriers with shape functions

The results of the previous section on the effect of shape functions on spectral free energies suggest a scheme by which free energy barriers can be 'flattened' in Monte Carlo simulations. In this section we outline the general principle according to which this can be achieved. To be specific, we consider here the flattening of spectral free energy barriers associated with *energy* histograms at a finite temperature.

Let $\mathcal{H}(x)$ denote the physical Hamiltonian under consideration, and $\mathcal{F}(E)$ the spectral free energy corresponding to the energy histogram $\mathcal{P}(E)$ of $\mathcal{H}(x)$. (In order to keep the notation simple, the subscript β, which indicated the inverse temperature in Eqs. (19)–(26), will be omitted in the fol-

lowing). It is clear already from a naïve point of view, that the ability to overcome free energy barriers corresponds to the – at least implicit knowledge of the function $\mathcal{F}(E)$. Let us therefore for the time being assume that we have already gained this knowledge, i.e., that $\mathcal{F}(E)$ is known. We now choose the *negative* spectral free energy $\mathcal{F}(E)$ itself as shape function, and adopt in Eq. (42) the identifications of variables $\mathcal{H}_1 \equiv \mathcal{H}$, $\mathcal{H}_2 \equiv \mathcal{H}_{\text{eff}}$, $\mathcal{A}(x) \equiv \mathcal{H}(x)$, $A \equiv E$, and the definition $f(E) := -\mathcal{F}(E)$. Thus we are dealing here with a 'non-physical' Hamiltonian

$$\mathcal{H}_{\text{eff}}(x) := \mathcal{H}(x) - \mathcal{F}[\mathcal{H}(x)], \quad (48)$$

which we will refer to as the *effective* Hamiltonian in this section. It is solely defined by the physical Hamiltonian $\mathcal{H}$ and depends – due to the temperature dependence of $\mathcal{F}$ – also on the (inverse) temperature. For the spectral free energy $\mathcal{F}_{\text{eff}}(E)$ associated with the effective Hamiltonian we obtain from Eq. (46)

$$\beta\mathcal{F}_{\text{eff}}(E) = K, \quad (49)$$

i.e., this spectral free energy is a (temperature-dependent) constant, and a (spectral) free energy barrier does not exist in this case.

Before we proceed to discuss the implications of this finding, it is instructive to consider again the the effective Hamiltonian $\mathcal{H}_{\text{eff}}$. In Section 2.1 we found a general relation between a Hamiltonian, the spectral free energy associated with the energy histogram, and the microcanonical entropy. By employing the current notation in Eq. (26), we obtain

$$\beta\mathcal{F}[\mathcal{H}(x)] = -S[\mathcal{H}(x)]/k_{\text{B}} + \beta\mathcal{H}(x) - \beta F, \quad (50)$$

and thus from Eq. (48) for the effective Hamiltonian the relation

$$\beta\mathcal{H}_{\text{eff}}(x) = S[\mathcal{H}(x)]/k_{\text{B}} + \beta F. \quad (51)$$

From this result we see that apart from a temperature-dependent constant βF ($F \equiv F_\beta$ in Eq. (48)) the effective Hamiltonian is identical to the microcanonical entropy $S[\mathcal{H}(x)]$. In a Monte Carlo simulation the Metropolis transition probability corresponding to this effective Hamiltonian would be given by

$$\pi(x_i \rightarrow x_j) = \min \left(1, e^{\left\{ S[\mathscr{H}(x_j)] - S[\mathscr{H}(x_i)] \right\}/k_B} \right), \qquad (52)$$

where the 'constant' βF does not appear in the exponent due to cancellation.

We now proceed to discuss a strategy to flatten free energy barriers which is a direct consequence of the results obtained so far. Since we do not know the spectral free energy $\mathscr{F}(E)$ in advance – its knowledge is essentially equivalent to the knowledge of the microcanonical entropy (cf., Eq. (51)) and therefore to the 'solution' of our problem – we have to resort to an *iterative* scheme by which a successively better knowledge of $\mathscr{F}(E)$ can be obtained. This iterative scheme can be outlined as follows:

Start with an initial approximation $\mathscr{F}^{(0)}(E)$ for $\mathscr{F}(E)$. During a series of simulations, determine successively better approximations $\mathscr{F}^{(1)}(E)$, $\mathscr{F}^{(2)}(E)$, ..., $\mathscr{F}^{(n)}(E)$, ..., where $\mathscr{F}^{(n)}(E)$ converges towards $\mathscr{F}(E)$ with increasing iteration index n. A single iteration cycle can be described as follows.

By employing the approximation $\mathscr{F}^{(n-1)}(E)$ (obtained in the previous cycle) as new shape function, a better approximation for the effective Hamiltonian $\mathscr{H}_{eff}$ can be defined as

$$\mathscr{H}_{eff}^{(n)}(x) := \mathscr{H}(x) - \mathscr{F}^{(n-1)}[\mathscr{H}(x)]. \qquad (53)$$

A simulation with Boltzmann sampling with respect to $\mathscr{H}_{eff}^{(n)}(x)$ is then performed (which means non-Boltzmann sampling with respect to the original Hamiltonian $\mathscr{H}(x)$), and the energy histogram $\mathscr{P}_{eff}^{(n)}(E)$ is sampled. The associated spectral free energy $\mathscr{F}_{eff}^{(n)}(E)$ is subsequently determined. *If* the simulation would have been done with perfect statistics, $\mathscr{F}_{eff}^{(n)}(E)$ would be related to $\mathscr{F}(E)$ by $\mathscr{F}_{eff}^{(n)}(E) = \mathscr{F}(E) - \mathscr{F}^{(n-1)}(E) + \text{const.}$ However, as long as the free energy barrier has not been sufficiently flattened, the statistics will be inadequate because of an insufficient number of barrier crossings. Therefore the latter equation will not hold exactly, but only approximately. Solving for $\mathscr{F}(E)$ in the latter equation then yields $\mathscr{F}(E) \approx \mathscr{F}_{eff}^{(n)}(E) + \mathscr{F}^{(n-1)}(E) - \text{const.}$ As a better approximation for $\mathscr{F}(E)$ we therefore choose

$$\mathscr{F}^{(n)}(E) := \mathscr{F}_{eff}^{(n)}(E) + \mathscr{F}^{(n-1)}(E). \qquad (54)$$

Note that the constant is irrelevant – it only corresponds to a shift of the energy scale but does not change the shape of free energy barriers – and can be omitted. With this (better) approximation for $\mathscr{F}(E)$ a new simulation is then performed in the next iteration cycle.

During the course of the iteration, $\mathscr{H}_{eff}^{(n)}(x)$ will asymptotically approach the function $S[\mathscr{H}(x)]/k_B$ (apart from the unknown constant βF), and the spectral free energy barrier associated with $\mathscr{H}_{eff}^{(n)}$ will eventually be completely flattened, i.e., $\mathscr{F}_{eff}^{(n)}(E)$ will converge towards a constant value.

As reviewed in the introduction, our shape function method is just another variant of multicanonical sampling, and therefore the underlying strategy is essentially the same: By iteration non-Boltzmann weights are determined which asymptotically are proportional to the inverse density-of-states $\Omega(E)^{-1} = \exp[-S(E)/k_B]$ of the model system. In the standard formulation of the multicanonical ensemble technique, this is achieved by approximating the microcanonical entropy within successive energy subintervals $E_k \leqslant E < E_{k+1}$ piecewise by linear segments $S(E) \simeq [S(E_k) - S'(E_k) \cdot E_k] + S'(E_k) \cdot E$ (with $S'(E_k) \equiv dS(E)/dE|_{E_k}$). This corresponds to an effective Hamiltonian which inside each energy subinterval is defined by $\beta\mathscr{H}_{eff}(x) \simeq \alpha_k + \beta_k \mathscr{H}(x)$ (for $E_k \leqslant \mathscr{H}(x) < E_{k+1}$). The parameters α_k and β_k, of which the latter are related to the local (average) derivative of the entropy by $\beta_k = S'(E_k)/k_B$ (which gave rise to the term 'multicanonical' in the sense that there is a different fictitious temperature defined for each energy subinterval) are then determined in an automated iterative way. From a technical point of view there is no reason to assume that our shape function approach is superior to the multicanonical or the entropic sampling technique in the sense that it will produce more accurate results, or that these could be obtained with less computational effort. What we would like to emphasize, however, is the simplicity and the resulting transparency of our approach regarding its physical interpretation. This may also help to adapt it more easily to systems of more complex nature.

3.3. Implementation of the shape function method

An application of the iteration scheme outlined in the previous subsection to specific model systems involves also the consideration of implementation details of a more technical character. In this section some of these issues will be briefly addressed. More details will be presented in two case studies (Section 4).

The height of free energy barriers between coexisting phases increases with the linear system size L according to a power law (cf. the discussion in Section 2.3 and Eq. (41)). Consequently a good sampling statistics can be more easily obtained in simulations of systems with a relatively small system size. It is therefore recommended to start the iteration with a small system size L_1, for which already after one iteration cycle a sufficiently good approximation of the spectral free energy $\mathscr{F}_{L_1}(E)$ can be obtained (the iteration index n is omitted here). By taking the results of Section 2.3 for the system size dependence of free energy barriers into account, $\mathscr{F}_{L_1}(E)$ may then be used to obtain an approximate spectral free energy $\mathscr{F}_{L_2}(E)$ for a slightly bigger system size $L_2 > L_1$. Since also the transition temperature T_t is L-dependent, a reweighting step has to be inserted to obtain the free energy $\mathscr{F}_{L_2}(E)$ at the transition temperature $T_t(L_2)$ for the new system size. The iteration scheme is then resumed for the new system size L_2. By including repeatedly extrapolation steps from smaller to bigger system sizes and a subsequent reweighting step, the iteration is then continued until a sufficiently big system size is reached.

Another highly relevant aspect of the implementation of the method is to avoid a waste of computer time by preventing the system to explore regions of the phase space which are more or less irrelevant for the phenomenon which is to be studied in the simulations. A Boltzmann simulation with respect to the asymptotic effective Hamiltonian $\mathscr{H}_{\text{eff}}$ would generate a one-dimensional random walk on the energy axis, because the spectral free energy $\mathscr{F}_{\text{eff}}(E)$ is constant in that case. (Here and in the following discussion the label L for the system size and the iteration index n are suppressed to allow for a better readability).

While this is favorable for parts of the phase space corresponding to the 'connecting states' between the ordered phase and the disordered phase (i.e., for energy values $E_t^- < E < E_t^+$ in the terminology used in Section 2.3), regions of the phase space corresponding to energies $E \ll E_t^-$ and $E \gg E_t^+$, respectively, should be excluded in the simulations. This can be achieved by explicitly preventing the system from entering these regions by defining 'repulsive walls' on the energy axis which limit the accessible energy values essentially to the interval $E_t^- - \varepsilon < E < E_t^+ + \varepsilon$, where ε is a small energy increment which can be adjusted to obtain good statistics around the minima $E_t^\pm$ of $\mathscr{F}(E)$. Alternatively also a slightly modified shape function $\tilde{\mathscr{F}}(E)$ can be employed which attempts to flatten only the free energy barrier between the ordered and the disordered phase but leaves the spectral free energy for $E < E_t^-$ and $E > E_t^+$ unmodified. It can be defined by

$$\tilde{\mathscr{F}}(E) := \begin{cases} \mathscr{F}(E_t^-) & \text{for } E < E_t^-; \\ \mathscr{F}(E) & \text{for } E_t^- \leqslant E \leqslant E_t^+; \\ \mathscr{F}(E_t^+) & \text{for } E_t^+ < E. \end{cases} \qquad (55)$$

A last point to be mentioned here is the way how an approximate spectral free energy $\mathscr{F}(E)$ (obtained in the simulation of the previous iteration cycle) is actually implemented in the computer code for the subsequent simulation. In cases, where the discrete energy values of the model system are more or less homogeneously distributed in the relevant energy interval, it is recommended to implement the spectral free energy directly as a histogram. For a given microconfiguration x, the energy $E \equiv \mathscr{H}(x)$ is then evaluated in the simulation, and the number of the bin to which this energy value belongs is determined. For this bin number the (approximate) spectral free energy value $\mathscr{F}(E)$ can then be retrieved. In cases where the energy values are more inhomogeneously distributed, on the other hand, it may be more useful to store all energy values without binning during the simulation. By means of a data fit the numerical parameters of a suitable interpolating function can then be calculated. This interpolating function can then be directly used to evaluate $\mathscr{F}(E)$ in the next iteration cycle.

4. Applications

In this section we discuss two applications of the non-Boltzmann sampling technique with shape functions in order to illustrate its potential. In the first case study the technique is utilized to overcome the free energy barrier between competing low- and high-temperature phases in a two-dimensional lattice model designed to describe binary lipid bilayers. In combination with Lee–Kosterlitz scaling, the interfacial tension between the two phases is determined. In the second application, non-Boltzmann sampling is employed to a two-dimensional lattice gas 'toy' model which exhibits interfacial melting (grain-boundary melting) for certain types of domain interfaces. Here the focus is on a precise determination of the bulk transition temperature, which is a prerequisite for the study of the scaling behavior of the width of the interfacial wetting layer. Practical aspects of implementation of the technique are discussed, and the main results are presented.

4.1. Phase equilibria in binary lipid bilayers

Phase transitions and phase equilibria in soft condensed matter systems are notoriously difficult to study by simulation methods because they are strongly influenced by the vast conformational complexity and fluctuations that characterize the long-chain molecules which make up soft matter. Examples include polymer systems and supra-molecular aggregates of amphiphiles, e.g., lipid bilayers which are important models of biological membranes. Lipid bilayers have a series of phase transitions, one of which, the so-called main phase transition, taking place at a temperature T_t, is predominantly a chain-melting process [98]. We shall in this section be concerned with this phase transition and the associated phase equilibria in binary lipid mixtures made up of saturated di-acyl phosphatidylcholines, DC_nPC, where n denotes the number of carbon atoms in each of the two acyl chains.

The nature of the main phase transition in pure lipid bilayers is a controversial issue. It is believed to be a first-order phase transition driven by the internal entropy of the lipid-acyl chains [98]. There is, however, no clear-cut experimental evidence for the first-order nature, and the current consensus is that for not too long chains, $n \simeq 16$, the transition is probably a very weak first-order transition associated with strong fluctuation effects [99,100]. Some model calculations have suggested that there is a critical point around $n \leqslant 18$, with no phase transitions for shorter chains and first-order phase transitions for longer chains [101,102]. The position of the critical point is however very dependent on details in the models as well as on small amounts of a second component [102]. We shall not go further into the question as to what the true nature of the phase transition is in real lipid membranes but here show how the simulation techniques described in the present paper can be useful to accurately determine the phase transition and the phase equilibria in a specific model of the main phase transition in lipid bilayers. For further discussion of models specifically designed to elucidate deeper details of the phase transition the reader is referred to Ref. [103].

4.1.1. Lattice-gas model and binary phase diagram

The model we shall study is an extension of the ten-state Pink model for one-component lipid bilayers [104] designed to describe the main phase transition by focussing on the internal degrees of freedom of the acyl chains. The Pink model is formally a lattice gas model, where each site of the lattice is assigned a multi-state variable, m, which reflects the conformational states of the chain at that site. Each monolayer of the bilayer is represented by a triangular lattice and the two monolayers are assumed not to interact. Pink and collaborators originally chose ten states, $m = 1, \ldots, 10$ (for reasons of comparison with certain spectroscopic data), each of which is characterized by an internal conformational energy, E_m, a cross-sectional area, A_m, and an internal entropy, $k_B \ln D_m$, reflecting that each state may be degenerate and representing a number, D_m, of different molecular configurations with the same area and internal energy. It is this internal degeneracy that underlies the transitional phenomena. The cross-sectional area is reciprocally related to the hydrophobic length, d_m, of the chain (by volume conservation). Nine of the ten states are characteristic of the low-temperature

conformationally ordered phase (the so-called gel phase) and the tenth state is characteristic of the high-temperature, conformationally disordered (melted) state (the so-called fluid phase). The states are coupled by van der Waals interactions and the system is furthermore subject to an interfacial lateral pressure, Π, to assure bilayer stability.

In terms of these variables, the lattice-gas Hamiltonian for the Pink model for a one-component system (lipid species A) can be written

$$\mathcal{H}^A\{c_{im}^A\} = \sum_i \sum_{m=1}^{10} (E_m^A + \Pi A_m^A)c_{im}^A$$
$$- \frac{J_A}{2} \sum_{\langle i,j \rangle} \sum_{m,m'=1}^{10} I_m^A I_{m'}^A c_{im}^A c_{jm'}^A. \quad (56)$$

$c_{im}^A \in \{0,1\}$ is an occupation variable for site i, subject to the sum rule $\sum_m c_{im}^A = 1$, which is 1 if the acyl chain on site i is in state m, and 0 otherwise. I_m^A is a product of a term related to the van der Waals interaction between chains and a phenomenological expression for the shape-dependent nematic order parameter [104]. The model is in principle a semi-phenomenological molecular interaction model and its various parameters, e.g., the strength parameter J^A, have to be determined independently (see Ref. [105]).

This model can now be extended to a binary mixture of two species, A and B, as

$$\mathcal{H}\{c_{im}^A, c_{jm'}^B\} = \mathcal{H}^A\{c_{im}^A\} + \mathcal{H}^B\{c_{im}^B\}$$
$$+ \mathcal{H}^{AB}\{c_{im}^A, c_{jm'}^B\} + \mu \sum_i \sum_{m=1}^{10} c_{im}^B, \quad (57)$$

where μ is a chemical potential that controls the composition of the mixture in the grand-canonical ensemble. The occupation variables c_{im}^A and c_{im}^B now have to obey the modified sum rule $\sum_m (c_{im}^A + c_{im}^B) = 1$. The interaction between different lipid species is described by the symmetrized Hamiltonian [106]

$$\mathcal{H}^{AB}\{c_{im}^A, c_{jm'}^B\}$$
$$= \sum_{\langle i,j \rangle} \sum_{m,m'=1}^{10} \left[-\frac{J_{AB}}{2} (I_m^A I_{m'}^B c_{im}^A c_{jm'}^B + I_m^B I_{m'}^A c_{im}^B c_{jm'}^A) \right.$$
$$\left. + \frac{\Gamma}{2} (|d_{im}^A - d_{jm'}^B|c_{im}^A c_{jm'}^B + |d_{im}^B - d_{jm'}^A|c_{im}^B c_{jm'}^A) \right]. \quad (58)$$

The first term in $\mathcal{H}^{AB}$ describes the direct van der Waals hydrophobic contact interaction between different acyl chains. The corresponding interaction constant is taken to be the geometric average $J_{AB} = (J_A J_B)^{1/2}$. Γ in the second term of the equation represents the so-called hydrophobic mismatch interaction and is assumed to be universal in the sense that its value does not depend on acyl-chain length. The values of the various model parameters are described in Ref. [102].

We shall here use this model to investigate the phase equilibria in a binary mixture composed of two lipid species which only differ with respect to the lengths of the acyl chains, specifically $DC_{14}PC$, $DC_{16}PC$, and $DC_{18}PC$. The phase diagram of the model for $DC_{14}PC$–$DC_{18}PC$ mixtures, calculated as described below, is shown in Fig. 1. It contains a massive region of gel-fluid phase coexistence and an almost horizontal solidus line, reflecting the very non-ideal mixing behavior of this mixture. This diagram is in close correspondence with experimental data [106].
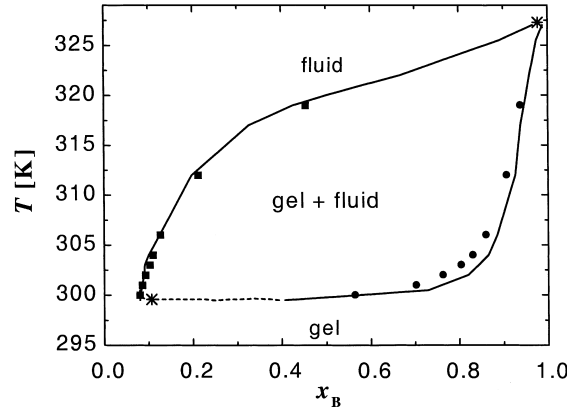

Fig. 1. Phase diagram of $DC_{14}PC$–$DC_{18}PC$ lipid mixtures in the temperature-composition plane. x_B is the relative concentration of $DC_{18}PC$ as defined in the text. The solid lines are obtained from conventional Monte Carlo sampling for a series of small system sizes, $L = 10 - 15$. The data points are obtained by non-Boltzmann sampling as described in the text and refer to simulations on system sizes in the range $L = 40 - 60$. Two asterisks (∗) denote the upper and lower critical mixing points, respectively.

4.1.2. Implementation of the shape function method

In order to determine the phase diagram in the temperature-composition plane we chose a grand-canonical ensemble where the composition, $x_B = L^{-2} \sum_i \sum_m \langle c_{im}^B \rangle$, is a fluctuating quantity. A histogram of compositions is then sampled and the corresponding spectral free energy, $\mathscr{F}_{1,\mu,T}(x_B)$, is analyzed at $\mu = \mu_t$ and T corresponding to coexistence.

The shape function method is invoked by sampling according to the modified Hamiltonian

$$\mathscr{H}_{\text{eff}}\{c_{im}^A, c_{jm'}^B\} = \mathscr{H}\{c_{im}^A, c_{jm'}^B\} + f(\hat{x}_B), \qquad (59)$$

where $\hat{x}_B = L^{-2} \sum_i \sum_m c_{im}^B$ is the operator which returns the composition on the lattice. The use of this operator reflects the fact that data obtained from simulation of one system size may serve as input to simulation of another system size. The shape function $f(\hat{x}_B)$ is chosen such that the corresponding spectral free energy function $\mathscr{F}_2(x_B)$ is flat in the interval $x_1 \leqslant x_B \leqslant x_2$ corresponding to coexistence. As described in Section 3.3, this is done by choosing $f(x_B)$ as a smooth function which is equal to $-\mathscr{F}_1(x_B) + \text{const}$ inside the interval of coexistence and constant outside.

The use of the modified Hamiltonian Eq. (59) requires prior knowledge of the spectral free energy function $\mathscr{F}_1(x_B)$ which is obtained in a approximate way using a finite-size scaling-estimate of $\mathscr{F}_1(x_B)$. This is achieved by the following five-step iteration procedures:

(i) For a given temperature, T, the chemical potential of coexistence, μ_t, and the corresponding spectral free energy function $\mathscr{F}_1(x_B)$ are estimated for a system of size L_q, where q enumerates the different system sizes considered.

(ii) A Monte Carlo simulation is performed using the modified Hamiltonian Eq. (59) in order to obtain the corresponding function $\mathscr{F}_2(x_B)$.

(iii) A reweighting, using $\mathscr{F}_1(x_B) = \mathscr{F}_2(x_B) - f(x_B)$, cf. Eq. (46), is performed in order to obtain the spectral free energy function according to the physical Hamiltonian.

(iv) A Ferrenberg–Swendsen reweighting, cf., Eq. (32), is carried out in order to obtain the chemical potential μ_t and $\mathscr{F}_1(x_B)$ corresponding to coexistence.

(v) The steps from (ii) are repeated in order to improve the sampling of $\mathscr{F}_1(x_B)$ for the same system size, or alternatively a larger system, L_{q+1}, is considered by starting at (i) again.

When increasing the system size from L_q to L_{q+1}, the approximate scaling relation

$$\mathscr{F}_{1,L_{q+1}}(x_B) \approx \frac{L_{q+1}}{L_q} \mathscr{F}_{1,L_q}(x_B) \quad (x_1 \leqslant x_B \leqslant x_2) \qquad (60)$$

for two-dimensional systems with first-order transitions is assumed to hold. Furthermore, it is assumed that the chemical potential, μ_t, corresponding to coexistence and the locations of the minima x_1 and x_2 are independent of the system size. Obviously these assumptions are only approximately correct, and in practice, the possible error sets a limit for how much the system size can be increased in step (i).

The simulations are carried out using the standard Monte Carlo Metropolis algorithm [97]. Thermal equilibrium of the model system is attained using single-site Glauber excitation for the acyl-chain degrees of freedom for each lipid species. Equilibrium with the particle reservoir within the grand canonical ensemble is simulated by single-site conversion of the lipid species and simultaneous assignment of a random conformation of the involved acyl chain. The finite lattices used are subject to periodic boundary conditions. The statistics required to accurately determine the phase coexistence at a given temperature typically involves $10^6 - 10^7$ Monte Carlo steps per lattice site.

4.1.3. Results

We shall now show results for the phase equilibria in a binary lipid mixture of $DC_{14}PC$ (henceforth referred to as lipid species A) and $DC_{18}PC$ (lipid species B), described by the ten-state Pink model in Eq. (57). From previous simulations using both histogram and finite-size scaling techniques [102,107], it is known that lipid bilayers of $DC_{14}PC$ and $DC_{18}PC$ described by this model do not display a phase transition in a strict thermodynamic sense but undergo a continuous, non-singular transformation within a very narrow temperature range. However, mixing one compo-
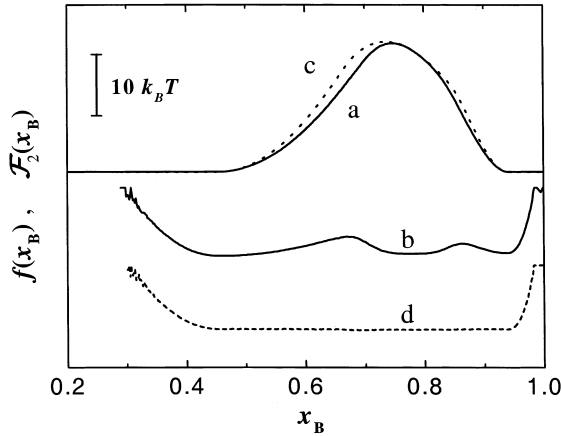
Fig. 2. Illustration of the use of shape functions to flatten a free-energy barrier obtained in simulations on the model of $DC_{14}PC$–$DC_{18}PC$ lipid mixtures. The figure shows data obtained from simulation of the model for a binary lipid mixture at a temperature ($T = 319$ K) near phase coexistence. (a) Shape function $f(x_B)$ for $L = 25$, obtained from finite-size scaling of $\mathscr{F}_1(x_B)$ from a previous simulation on a smaller system of size $L = 20$. (b) Partially flattened non-physical spectral free energy, $\mathscr{F}_2(x_B)$, obtained using the shape function in (a). (c) Shape function, $f(x_B)$, for a second simulation obtained using data from the first simulation. (d) Effectively flattened non-physical free energy function, $\mathscr{F}_2(x_B)$, obtained using the shape function in (c).

Fig. 3. Spectral free energy function, $\mathscr{F}_{1,\mu_t}(x_B)$, at phase coexistence for $DC_{14}PC$–$DC_{18}PC$ lipid mixtures at $T = 319$ K and for varying system sizes, $L = 5$–40 in steps of 5. The functions are obtained using the iteration scheme described Section 4.1.2.

nent into another can restore the first-order transition [102].

Fig. 2 shows data from two simulations on the modified Hamiltonian, Eq. (59), both performed at a temperature $T = 319$ K using a system size of $L = 25$. Fig. 2(a) shows a trial shape function estimated from the physical spectral energy corresponding to a smaller system of size $L = 20$. The trial shape function is not sufficiently accurately chosen and the resulting non-physical spectral free energy function, $\mathscr{F}_2(x_B)$, in Fig. 2(b) is therefore not completely flat, but shows two bumps in the middle. From the data of this first simulation a better shape function, cf. Fig. 2(c), has been constructed resulting in a more flat non-physical spectral free energy function as seen in Fig. 2(d).

Fig. 3 shows the physical spectral free energy function, $\mathscr{F}_{1,\mu_t}(x_B)$, for a temperature $T = 319$ K and a chemical potential μ_t corresponding to coexistence. The data are obtained by reweighting of
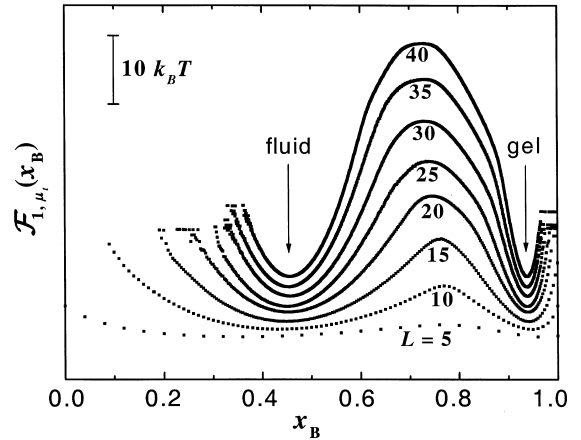
the spectral free energy function $\mathscr{F}_2(x_B)$ (cf., Fig. 2) corresponding to a Hamiltonian modified with a shape function. The figure shows spectral free energy functions with a barrier that increases strongly with the system size. This behavior suggests that the system exhibits a first-order transition corresponding to coexistence of two lipid phases with the compositions $x_B = 0.46$ and $x_B = 0.93$. The barrier height for the largest system, $L = 40$, studied at this temperature is about $32 k_B T$. In the case of a conventional simulation using the physical Hamiltonian this corresponds to the system being $e^{32} \approx 10^{14}$ times more likely to be found in one of the two minima than on top of the barrier. For a typical Monte Carlo simulation of 10^7 steps per site, it would therefore be virtually impossible to sample any configurations corresponding to energies at the barrier, and it would therefore also be practically impossible for the system to cross the barrier without modifying the Hamiltonian. For this temperature, $T = 319$ K, where the system shows a strong first-order behavior, a system size of $L = 11$ was found to be the upper limit for which conventional sampling could be used in practice.

From data like that presented in Fig. 3 the full phase diagram in the temperature-composition plane can be constructed as shown in Fig. 1. This
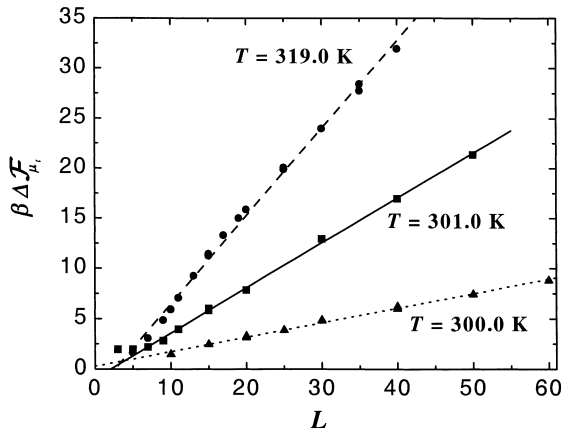
Fig. 4. Free-energy barrier height, $\Delta\mathcal{F}_{\mu_t}$, as function of the linear system size, L, for DC$_{14}$PC–DC$_{18}$PC lipid mixtures at different temperatures. From the slope of the linear relationships, the interfacial tension at phase coexistence, γ_t, are derived as shown in Fig. 5.
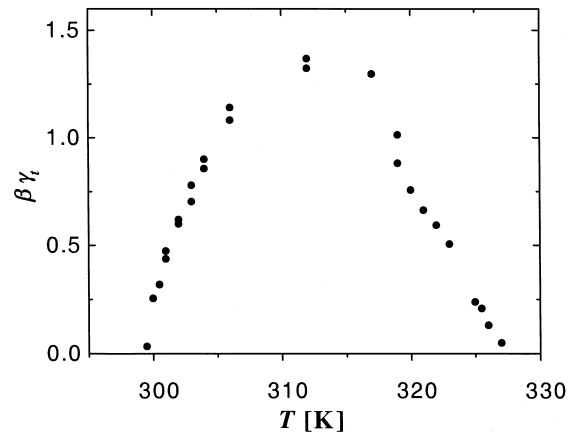

Fig. 5. Interfacial tension, γ_t, at phase coexistence for DC$_{14}$PC–DC$_{18}$PC lipid mixtures at different temperatures, obtained for system sizes in the range $L = 40 \ldots 60$. γ_t tends towards zero at the two critical mixing points, cf. the phase diagram in Fig. 1.

diagram shows that the coexistence region terminates in two critical mixing points near the pure limits.

Fig. 4 shows a scaling plot of the barrier height $\Delta\mathcal{F}_{\mu_t}$ as a function of the linear system size, L. The data display linear relationships for all temperatures in the coexistence region, and the surface tension, γ_t, between the two coexisting phases can therefore be obtained from the slope of the lines. The temperature dependence of γ_t is shown in Fig. 5. This figure illustrates how the interfacial tension vanishes as the critical mixing points are approached.

Some aspects of sampling a two-dimensional histogram are illustrated in Fig. 6. The data in this figure originates from simulations on a DC$_{14}$PC–DC$_{16}$PC mixture which is less non-ideal than DC$_{14}$PC–DC$_{18}$PC considered above and therefore has a more narrow co-existence region associated with relatively lower free energy barriers. The figure shows that a successful attempt to flatten, by the shape function method, the free energy barrier in terms of one variable, e.g., composition, does not remove the barrier in terms of another variable, e.g., energy. Comparison of Fig. 6(b) and (c) shows that even if the barrier effectively has been removed in (b) a large barrier of about $8k_BT$ remains in (c).

4.2. Lattice-gas model exhibiting interfacial melting

'Interfacial melting' is the phenomenon that – depending on material properties and thermodynamic parameters – melting in a multi-domain configuration of a condensed phase may start, at certain types of interfaces (grain-boundaries), already at temperatures below the bulk melting temperature T_t [108–110]. It is characterized by the appearance of a disordered, liquid-like interfacial 'wetting' layer which diverges in width when T_t is approached from below. From a theoretical point of view, interfacial melting is a special case of 'complete wetting' [110–112]. Contrary to the well developed theoretical understanding of the phenomenon, both the experimental and the simulational characterization of interfacial melting are in a somewhat unsatisfactory state mainly due to the extremely narrow temperature range over which the effect appears [113].

In this context a precise knowledge of the bulk melting temperature T_t (for given pressure or chemical potential) is imperative for a consistent interpretation of computer simulation (as well as experimental) data. Interfacial melting is usually associated with pronounced hysteresis effects visible in temperature scans over T_t, which makes the determination of T_t a non-trivial task.
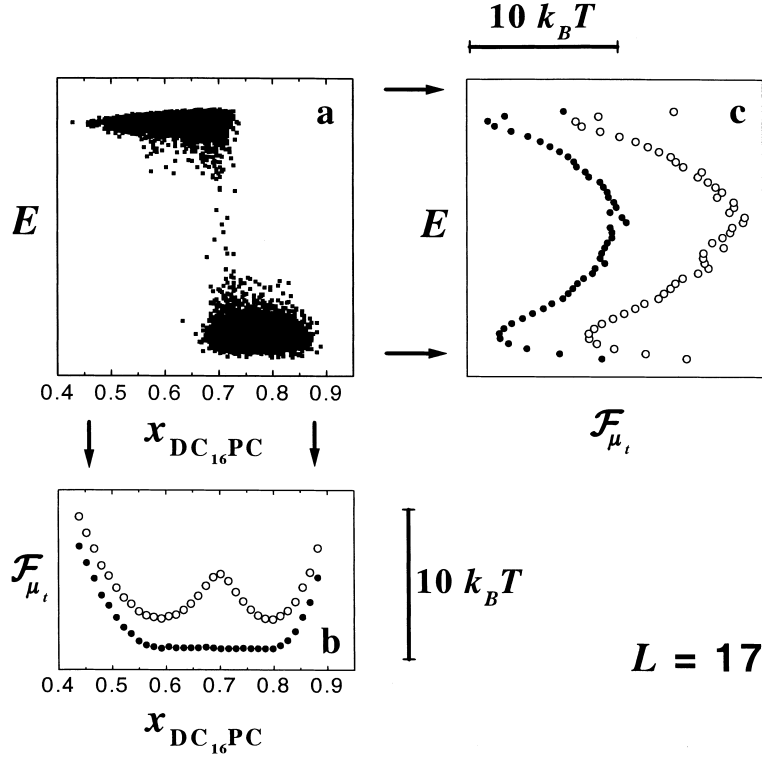
Fig. 6. Simulation data for a $DC_{14}PC$–$DC_{16}PC$ lipid mixture for a system of size $L = 17$ at a temperature of $T = 308$ K which is in between the transition temperatures of the two pure lipid species. (a) A subset of the raw energy data, E, for different compositions. (b) The spectral free energies, $\mathcal{F}_{\mu_t}(x_{DC_{16}PC})$, corresponding to the data in (a) in the case of use of a shape function (solid circles) and after reweighting the data to correspond to the physical Hamiltonian (open circles). (c) The spectral free energies, $\mathcal{F}_{\mu_t}(E)$, corresponding to the raw data in (a) (open circles) and to the data where a flattening of $\mathcal{F}_{2,\mu_t}(x_{DC_{16}PC})$ has been achieved, cf. (b).

In the following we report on the application of Monte Carlo histogram sampling with shape functions to a two-dimensional lattice gas model which exhibits interfacial melting. Since this application of the technique was primarily aimed at obtaining a good estimate for T_t, results concerning the interfacial melting effect itself will only be briefly mentioned. Details can be found elsewhere [114,115].

We first introduce the lattice-gas model and present its equilibrium phases and the corresponding phase diagram. We then proceed to a discussion of the computational procedures employed for sampling the histograms and for the implementation of the shape functions. We conclude with a discussion of the finite-size-scaling results for the bulk melting temperature.

4.2.1. Lattice-gas model and phase diagram

On a square lattice with N sites, an occupation variable $c_i \in \{0, 1\}$ is assigned to each site 'i'. The grand-canonical Hamiltonian of the system is given by

$$\mathcal{H}\{c_i\} = -\sum_{n=1}^{5} \varepsilon_n \sum_{\langle i,j \rangle_n} c_i c_j - \mu \sum_{i=1}^{N} c_i, \qquad (61)$$

where μ is the chemical potential and the interaction parameter for pairs $\langle i, j \rangle_n$ of occupied nth-nearest-neighbor sites (with $1 \leqslant n \leqslant 5$) is given by ε_n. By choosing $\varepsilon_1 = \varepsilon_2 = \varepsilon_3 = -\infty$ (repulsive hard-core interaction) and $\varepsilon_4, \varepsilon_5 > 0$ (attractive interactions) with $\varepsilon_4 = 1.2\varepsilon_5$, we obtain a lattice-gas model which was studied by Orban et al. [116].

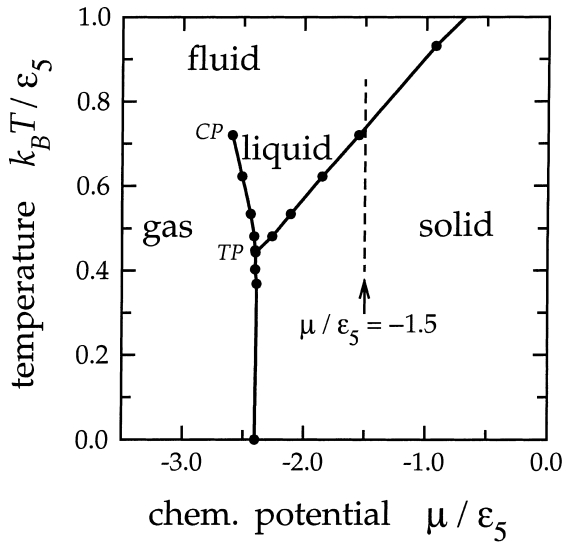The phase diagram (Fig. 7) of the model resembles that of a simple fluid system: it exhibits

Fig. 7. Chemical potential vs. temperature phase diagram of the lattice-gas model described by Eq. (61), as derived in Ref. [116] for a lattice strip of size $10 \times \infty$ with the transfer matrix method. 'TP' denotes the triple point of the gas, liquid, and solid phase, and 'CP' the Ising-type critical point of the liquid-gas transition. In the investigation reported in the present paper, the melting of the solid phase was studied at fixed chemical potential by varying the temperature (although for lattices with square aspect ratio $L \times L$, see text), as indicated by the dashed vertical line.

Fig. 8. Structure of the 'solid' phase. A domain is shown with positive rotation angle $(+\arctan 1/2)$ of the square super-structure unit mesh (with linear size $\sqrt{5}a$) with respect to the underlying square lattice (with lattice constant a). The figure shows the lattices sites (dots), the occupied sites (solid circles), and the associated 'atomic' hard-core disks (gray circles).

disordered 'lattice-gas' and 'lattice-liquid' phases, and a 'solid' phase. The latter has a '$(\sqrt{5} \times \sqrt{5})$R $\pm$ arctan 1/2' superstructure [117] with a square unit mesh of size $\sqrt{5} \times \sqrt{5}$ which is rotated by an angle $\pm\arctan1/2$ with respect to the underlying square lattice (Fig. 8). For either sign of the rotation angle, five 'out-of-phase' domain types exist which are related by translations. Thus the solid phase has a 10-fold degenerate groundstate with a corresponding manifold of different types of domain boundaries.

A major finding of extensive Monte Carlo simulations of the melting of two-domain-configurations ('bicrystals') in constrained equilibrium for various types of domain interfaces is that interfacial melting could only be observed for interfaces between domains of *opposite* sign of the domain rotation angle [115]. The melting of a bicrystal with a high-angle (36.87°) symmetric tilt boundary in the [11] direction between a '+' and a
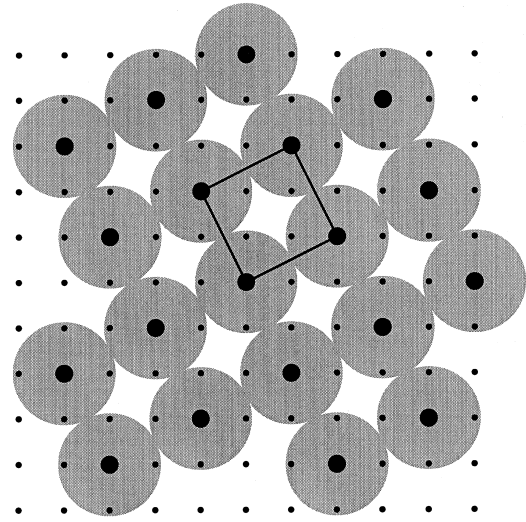
'−' domain at $\mu/\varepsilon_5 = -1.5$ has been studied in particular. Monte Carlo data over an extended temperature range indicate a logarithmic divergence of the width of the disordered wetting layer when the bulk melting temperature of the bicrystal is approached from below, in agreement with results of earlier mean-field studies [118]. The fact that a crossover to a power law divergence (as predicted by theory when interface fluctuations are taken into account) could not be observed has most probably to be attributed to the relatively small system sizes used in the bicrystal simulations [114].

Subsequent to the simulations of bicrystal melting, domain growth and its interference with interfacial melting in lattices without any constraints and square aspect ratio $L \times L$ were studied [115]. For this purpose the size-dependent bulk melting temperature $T_t(L)$ had to be determined in advance. Here non-Boltzmann sampling in combination with histogram reweighting and finite-size scaling for first-order transitions was employed as described in the next section.

4.2.2. Implementation of the shape function method

As discussed in the general outline of the iterative procedure to flatten a free energy barrier in Section 3.2, the most efficient approach is to start with a rather small system size and then proceed to increasingly bigger system sizes.

For very small system sizes, however, a general feature of many-particle systems may aggravate the binning of data associated with the sampling of histograms. The feature we refer to here is the considerably higher density of states at energies associated with disordered microconfigurations compared to the density of states at the lowest occurring energies, which are associated with well-ordered microconfigurations. Cases where this feature gives rise to quite pronounced effects for small system sizes include superstructures on a lattice like the solid phase of our lattice-gas model under consideration [119].

As a consequence the characteristic energy spacing between well-ordered states at low energies is much higher than the typical energy spacing between disordered states at elevated energy values, as can be seen from the normalized proba-bility distribution $\mathscr{P}_L(E)$ (where E denotes the energy per site) for $L = 10$ (Fig. 9). This distribution was obtained by first storing the energy values of the microconfigurations in the order of sequence as sampled during the simulation. After the simulation run was terminated, the sequence of obtained energy values was then sorted into ascending numerical order. In a last sweep over the ordered data sequence, the 'degeneracy' of numerically different energy values was determined. Clearly a simple binning of the energy values would not be adequate in this case since it would result in a distorted probability distribution. The relatively low number of discrete energy values, corresponding to well-ordered states, compared to the rather dense, but noisy distribution at higher energies also affects the determination of $T_t(L)$. The only applicable criterion to determine T_t in this case is the criterion of equal heights of the peaks corresponding to the two competing phases (ordered/disordered), but even then T_t can only be estimated with a relatively high uncertainty. Since the determination of T_t is done by a repeated combination of 'eye–balling' and reweighting the data (as outlined in Section 3.3), the corresponding spectral free energy $\mathscr{F}_L(E)$ (Fig. 10) turned out to be more helpful for this purpose from a subjective
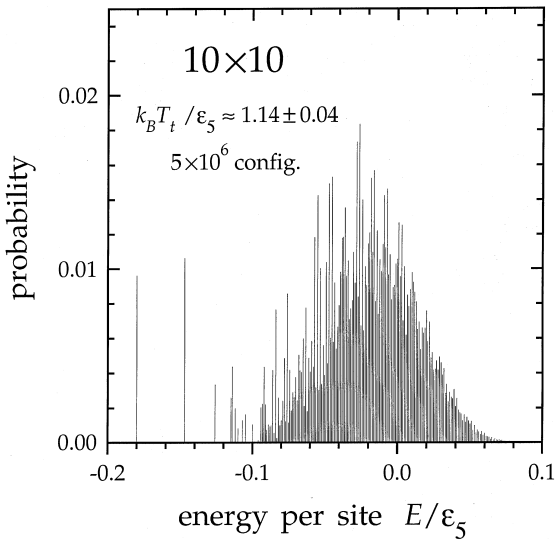

Fig. 9. Normalized probability distribution $\mathscr{P}_L(E)$ as function of the energy per site, E, for the system size $L = 10$ at the melting temperature $k_B T_t(L = 10)/\varepsilon_5 = 1.14 \pm 0.04$, as determined by the reweighting technique. The data were obtained at the chemical potential $\mu/\varepsilon_5 = -1.5$ by sampling over 5×10^6 equilibrium configurations.
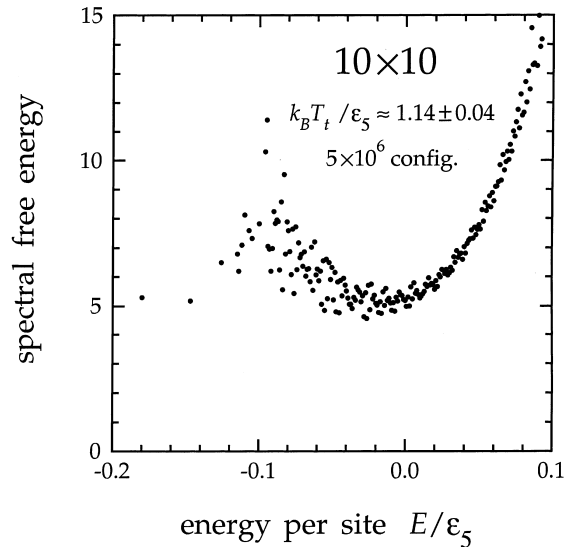

Fig. 10. Spectral free energy $\beta\mathscr{F}_L(E)/\varepsilon_5$ corresponding to the probability distribution in Fig. 9 for the system size $L = 10$.

point of view because of the lower scattering of the data points on a logarithmic scale. The uncertainty of the resulting estimate for T_t, however, can of course not be reduced by this choice.

We now address the implementation of the shape functions in this application. A first simulation with pure Boltzmann sampling was performed for a system of size $L = 10$ with an initial estimate for $T_t(L = 10)$. The resulting spectral free energy distribution was then reweighted by employing the equal-height criterion, resulting in a distribution with two minima at $E = E_+$ and $E = E_-$ (with $E_- < E_+$) at heights $\mathscr{F}_\pm$, and a maximum at $E = E_{\max} \approx (E_+ + E_-)/2$ with height $\mathscr{F}_{\max} > \mathscr{F}_\pm$. A truncated harmonic shape function of the form

$$f(E) = \frac{\mathscr{F}_{\max} + \mathscr{F}_\pm}{2} - \frac{\mathscr{F}_{\max} - \mathscr{F}_\pm}{2}$$
$$\times \cos\left[\frac{2\pi}{E_+ - E_-} (E - E_-) \right] \qquad (62)$$

for $E_- \leqslant E \leqslant E_+$ (and $f(E) = \mathscr{F}_\pm$ outside this interval) turned out to be a sufficiently good choice. It has the advantage that its parameters can be directly read off from a plot of the reweighted spectral free energy. It should be stressed that the use of the simple ansatz given by Eq. (62) is solely motivated by its simplicity. One might ask if it would not be preferable instead to choose a functional form which is derived from the physics of the problem, as discussed in Section 2.3. However, the precise form of the shape function does not matter as long as it ensures that a sufficiently high number of transitions between the two free energy minima can be achieved in the non-Boltzmann simulation with that shape function. For the same reason 'eye–balling' of the initial spectral free energy distribution is sufficient to get numerical values for the parameters of the shape function ansatz. In fact, a further refinement of the shape function turned out not to be necessary, and after a final reweighting procedure the distributions in Figs. 9 and 10 resulted, with an associated estimate for $T_t(L = 10)$.

The system size was then increased from 10 to 15. It should be emphasized that simulations were only performed for system sizes L which are an integer multiple of 5, because only in that case can

misfits of a completely ordered monodomain superstructure configuration on an $L \times L$ lattice with periodic boundary conditions be avoided [120]. The shape function for $L = 10$ was extrapolated to $L = 15$ as described in Section 3.3 and used as an initial shape function for non–Boltzmann sampling for the new system size. The resulting spectral free energy distribution was reweighted, and for the improved estimate of $T_t(L = 15)$ a new truncated harmonic shape function (according to Eq. (62)) was determined and subsequently used for a longer simulation (over 12×10^6 equilibrated MCS) for that system size. A final reweighting step led to the estimate $T_t(L = 15) = 0.883 \pm 0.002$.

The procedure as outlined above was repeated for increasing system sizes up to $L = 40$. Figs. 11 and 12 and show, respectively, the probability and the spectral free energy distribution for $L = 25$ at the estimated melting temperature for that system size. Note that although the 'disordered peak' of $\mathscr{P}_{25}(E)$ has already become quasi-continuous with only a minor amount of scattering (which allows a higher precision of the estimated melting temperature), there are still only relatively few discrete
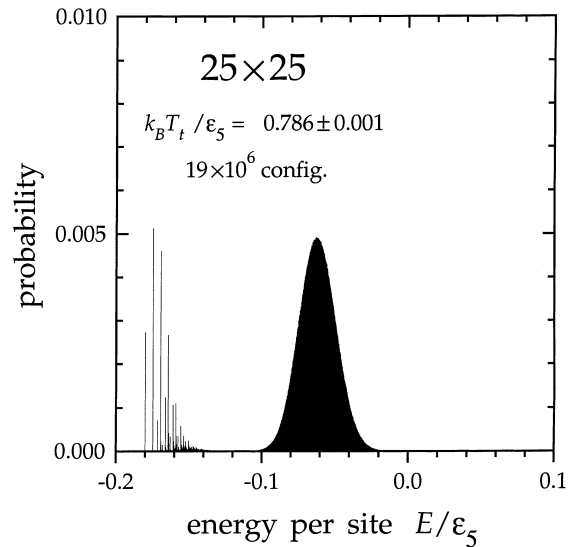

Fig. 11. Normalized probability distribution $\mathscr{P}_L(E)$ as function of the energy per site, E, for the system size $L = 25$ at the melting temperature $k_B T_t(L = 25)/\varepsilon_5 = 0.786 \pm 0.001$. The data were obtained at the chemical potential $\mu/\varepsilon_5 = -1.5$ by sampling over 19×10^6 equilibrium configurations.
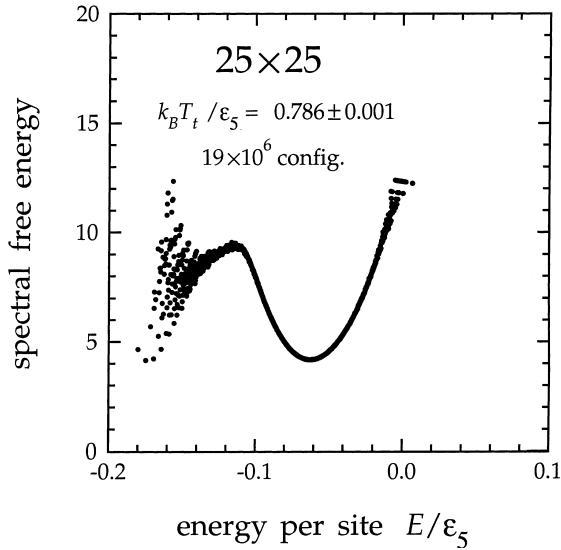
Fig. 12. Spectral free energy $\beta \mathscr{F}_L(E)/\varepsilon_5$ corresponding to the probability distribution in Fig. 11 for the system size $L = 25$.
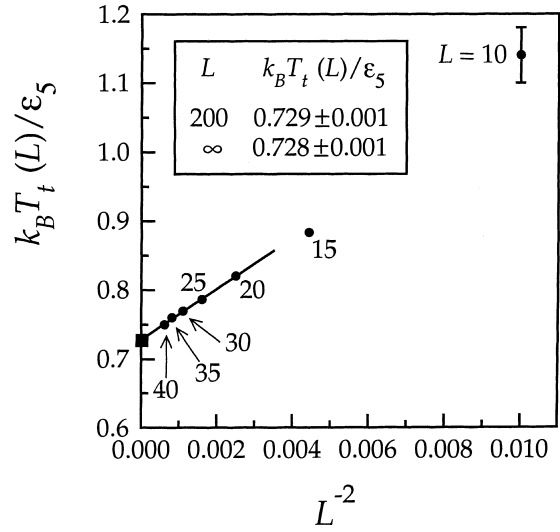

Fig. 13. Finite-size scaling plot of the system size dependent melting temperature $T_t(L)$ vs. the reciprocal number of lattice sites $N^{-1} = L^{-2}$. The data points (solid circles) refer to the results of simulations for the range $L = 10 \ldots 40$. The straight line is a fit of the expected scaling law (see text) to the data in the range $L = 20 \ldots 40$. The inset displays the extrapolated melting temperatures for the system size $L = 200$ and the infinite system size. (Note that the extrapolated points $(L^{-2}, T_t(L))$ for $L = 200$ and $L = \infty$ would be too close together to be discriminated in this plot; their location is marked by a solid square).

energy values which comprise the 'peak' of the ordered solid structure. Therefore binning of the data over the whole energy range would still not be adequate. However, with increasing system size the disordered peak will become more and more quasi-continuous in nature, and computer memory limitations will eventually require a procedure where at least the energy values belonging to the disordered peak have to be binned. Up to $L = 40$, however, the approach described above turned out to be sufficient.

4.2.3. Results

Here we report only two major results of the finite-size scaling analysis for our lattice-gas model. More detailed results will be published elsewhere [115].

For a first-order phase transition phenomenological finite–size scaling theory predicts the deviation of $T_t(L)$ from the infinite system melting temperature $T_t(\infty)$ to scale with the system 'volume' as L^{-d} [3], where d is the dimensionality of the system (here $d = 2$). Indeed the scaling plot of $T_t(L)$ vs. L^{-2} in Fig. 13 shows a fairly linear behavior for $L \gtrsim 15$. A fit of the function $T_t(L) = T_t(\infty) + aL^{-2}$ to the data results in the best fit value $k_B T_t(\infty)/\varepsilon_5 \approx 0.728 \pm 0.001$. For the

200×200 system we get an extrapolated value $k_B T_t(200)/\varepsilon_5 \approx 0.729 \pm 0.001$, which is in good agreement with the limits $0.728 < k_B T_t(200)/\varepsilon_5 < 0.730$ which were derived for this system size from simulations with a half-ordered/half-disordered initial configuration [115].

The spectral free energy barrier $\Delta \mathscr{F}(L)$ between the two competing phases at the corresponding finite-size melting temperature increases approximately linearly with the system size L as shown in Fig. 14. This clearly demonstrates the discontinuous character of the melting transition, although some of the occurring domain boundaries exhibit a continuous interfacial melting transition. In the case of periodic boundary conditions (with $r = 2$ in Eq. (41)), and under the assumption that the asymptotic behavior has already been reached for $L \gtrsim 20$, an (average) interfacial tension of $\gamma \approx 0.028 \, \varepsilon_5$ per lattice spacing results. This may be considered as a rather low value, and most probably simply reflects the rather small (and for $T \nearrow T_t$
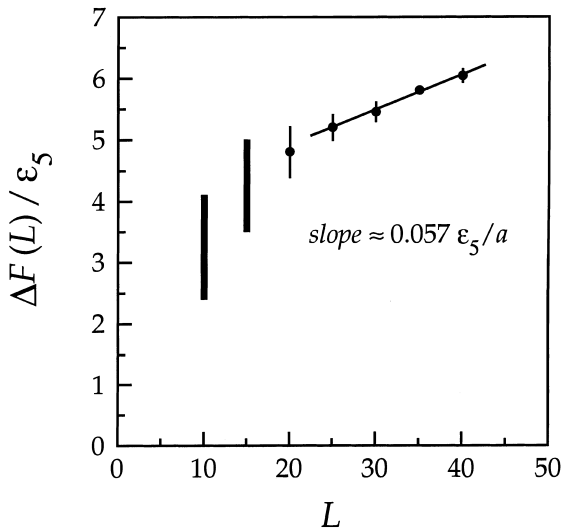
Fig. 14. Finite-size scaling plot of the spectral free energy barrier $\Delta\mathcal{F}(L)$ vs. the linear lattice size L. The bars for $L = 10$ and $L = 15$ reflect the fact that it is almost impossible to evaluate any well defined free energy barrier for these small system sizes. Fit of an affine-linear dependence (straight line segment) to the data points for $L > 20$ results in an effective surface tension of $\gamma \approx 0.028\,\varepsilon_5/a$.

vanishing) contributions to γ from domain interfaces which exhibit interfacial melting close to T_t.

5. Summary

In this paper we have demonstrated how free energy barriers associated with first-order phase transitions can be successfully dealt with by employing an iterative scheme which involves the use of effective Hamiltonians, which are obtained by adding suitable 'shape functions' to the physical Hamiltonian of the model system. By executing this procedure, an increasingly better knowledge of free energy barriers can be obtained, resulting in more efficient simulations with good statistics.

Our approach, which is based on the use of equilibrium probability distributions (histograms) and the associated 'spectral' free energies of fluctuating physical quantities, and includes histogram reweighting techniques as an essential part of the procedure, is transparent regarding its physical interpretation and it is simple in its technical implementation. Nonetheless, it offers sufficient flexibility for an easy adaption to specific model systems, as has been demonstrated by applying it to two lattice models, a binary lipid membrane model, and a crystal model which exhibits interfacial melting.

In this paper we limited the discussion to one-dimensional histograms and spectral free energies. The generalization of our approach to two- and higher-dimensional cases is in principle straightforward. However, other problems of general nature pertinent to these higher-dimensional cases may arise, e.g., how several free energy barriers of qualitatively different physical nature can be simultaneously flattened in an efficient way. It is our feeling, however, that problems like this can more likely successfully be dealt with using the versatile shape function approach than by employing other, technically more sophisticated non-Boltzmann sampling techniques, which may require more detailed considerations and modifications in order to apply them to specific model systems.

References

[1] K. Binder (Ed.), Monte Carlo Methods in Statistical Physics, 2nd ed., Springer, Berlin, 1986.
[2] K. Binder (Ed.), Applications of the Monte Carlo Method in Statistical Physics, 2nd ed., Springer, Berlin, 1987.
[3] K. Binder (Ed.), The Monte Carlo Method in Condensed Matter Physics, 2nd ed., Springer, Berlin, 1995.
[4] M.P. Allen, D.J. Tildesley, Computer Simulation of Liquids, Oxford University Press, Oxford, 1987 and 1989.

[5] D. Frenkel, B. Smit, Understanding Molecular Simulation, Academic Press, New York, 1996.

[6] O.G. Mouritsen, Computer Studies of Phase Transitions and Critical Phenomena, Springer, Berlin, 1984.

[7] K. Binder, C. Ciccotti (Eds.), Monte Carlo and Molecular Dynamics of Condensed Matter Systems (Como, July 1995), Società Italiana di Fisica, Bologna, 1996.

[8] M.P. Allen, D.J. Tildesley (Eds.), Computer Simulation in Chemical Physics, Kluwer Academic Publishers, Dordrecht, 1993.

[9] D.W. Heermann, Computer Simulation Methods, 2nd ed., Springer, Berlin, 1990.

[10] K. Binder, D.W. Heermann, Monte Carlo Simulation in Statistical Physics, Springer, Berlin, 1988.

[11] M. Plischke, B. Bergersen, Equilibrium Statistical Physics, 2nd ed., World Scientific, Singapore, 1994.

[12] S. Kirkpatrick, C.D. Gelatt Jr., M.P. Vecchi, Science 220 (1983) 671.

[13] B. Hesselbo, R.B. Stinchcombe, Phys. Rev. Lett. 74 (1995) 2151.

[14] A.P. Lyubartsev, A.A. Martinovski, S.V. Shevkunov, P.N. Vorontsov-Velyaminov, J. Chem. Phys. 96 (1992) 1776.

[15] E. Marinari, G. Parisi, Europhys. Lett. 19 (1992) 451.

[16] J. Lee, Phys. Rev. Lett. 71 (1993) 211.

[17] B.A. Berg, T. Neuhaus, Phys. Lett. B 267 (1991) 249.

[18] B.A. Berg, Phys. Rev. Lett. 68 (1992) 9.

[19] B.A. Berg, Int. J. Mod. Phys. C 3 (1992) 1083.

[20] B.A. Berg, Int. J. Mod. Phys. C 4 (1993) 249.

[21] B.A. Berg, in: F. Karsch, B. Monien, H. Satz (Eds.), Proceedings of the International Conference on Multiscale Phenomena and their Simulations (Bielefeld, October 1996), World Scientific, Singapore, 1997.

[22] W. Janke, Physica A 254 (1998) 164.

[23] B. Dünweg, in: K. Binder, C. Ciccotti (Eds.), Monte Carlo and Molecular Dynamics of Condensed Matter Systems (Como, July 1995), Società Italiana di Fisica, Bologna, 1996, p. 215.

[24] B.A. Berg, J. Stat. Phys. 82 (1996) 323.

[25] U.H.E. Hansmann, Phys. Rev. E 56 (1997) 6200.

[26] B.A. Berg, Nucl. Phys. B Proc. Suppl. 63 (1998) 982.

[27] B.A. Berg, U. Hansmann, T. Neuhaus, Phys. Rev. B 47 (1993) 497.

[28] B.A. Berg, U. Hansmann, T. Neuhaus, Z. Phys. B 90 (1993) 229.

[29] W. Janke, B. Berg, M. Katoot, Nucl. Phys. B 382 (1992) 649.

[30] W. Janke, Int. J. Mod. Phys. C 3 (1992) 1137.

[31] K. Rummukainen, Nucl. Phys. B 390 (1993) 621.

[32] C. Borgs, W. Janke, J. de, Physique I (Paris) 2 (1992) 2011.

[33] E. Buffenoir, S. Wallon, J. Phys. A 26 (1993) 3045.

[34] A. Billoire, T. Neuhaus, B. Berg, Nucl. Phys. B 413 (1994) 795.

[35] N.B. Wilding, Phys. Rev. E 52 (1995) 602.

[36] N.B. Wilding, M. Müller, J. Chem. Phys. 102 (1995) 2562.

[37] G.R. Smith, Europhys. Lett. 34 (1996) 91.

[38] G.R. Smith, Phys. Rev. E 53 (1996) 6530.

[39] B. Grossmann, Phys. Lett. B 293 (1992) 175.

[40] B. Grossmann, Int. J. Mod. Phys. C 3 (1992) 1147.

[41] B. Grossmann, M.L. Laursen, Nucl. Phys. B 408 (1993) 637.

[42] F. Karsch, T. Neuhaus, A. Patkós, Nucl. Phys. B 441 (1995) 629.

[43] F. Csikor, Z. Fodor, J. Hein, J. Heitger, Phys. Lett. B 357 (1995) 156.

[44] G. Arnold, T. Lippert, K. Schilling, Phys. Rev. D 59 (1999) 54509.

[45] B.A. Berg, Int. J. Mod. Phys. C 3 (1992) 1251.

[46] B. Berg, T. Celik, Phys. Rev. Lett. 69 (1992) 2292.

[47] T. Celik, Nucl. Phys. B Proc. Suppl. 30 (1993) 908.

[48] B.A. Berg, Europhys. Lett. 22 (1993) 63.

[49] U.H.E. Hansmann, Int. J. Mod. Phys. C 5 (1994) 85.

[50] B. Berg, U. Hansmann, T. Celik, Phys. Rev. B 50 (1994) 1644.

[51] B.A. Berg, Nucl. Phys. B Proc. Suppl. 34 (1994) 664.

[52] K.K. Bhattacharya, Phys. Rev. E 57 (1998) 2553.

[53] U.H.E. Hansmann, J. Phys. Soc. Jpn. 63 (1994) 3495.

[54] U.H.E. Hansmann, Nucl. Phys. B Proc. Suppl. 42 (1995) 914.

[55] N. Urakami, J. Phys. Soc. Jpn. 65 (1996) 2694.

[56] N. Nakajima, Chem. Phys. Lett. 278 (1997) 297.

[57] N. Nakajima, J. Phys. Chem. B 101 (1997) 817.

[58] H. Shirai, J. Molec. Biol. 278 (1998) 481.

[59] N. Nakajima, Chem. Phys. Lett. 288 (1998) 319.

[60] U.H.E. Hansmann, J. Phys. Chem. B 102 (1998) 653.

[61] U.H.E. Hansmann, J. Comp. Chem. 14 (1993) 1333.

[62] M.H. Hao, H.A. Scheraga, J. Phys. Chem. 98 (1994) 4940.

[63] U.H.E. Hansmann, Physica A 212 (1994) 415.

[64] U.H.E. Hansmann, Int. J. Mod. Phys. C 5 (1994) 93.

[65] Y. Okamoto, J. Phys. Chem. 99 (1995) 11276.

[66] U.H.E. Hansmann, Phys. Rev. E 54 (1996) 5863.

[67] U.H.E. Hansmann, Nucl. Phys. B Proc. Suppl. 47 (1996) 842.

[68] J. Higo, J. Comp. Chem. 18 (1997) 2086.

[69] U.H.E. Hansmann, J. Chem. Phys. 110 (1999) 1267.

[70] J. Lee, Phys. Rev. E 50 (1994) R651.

[71] U.H.E. Hansmann, B.A. Berg, T. Neuhaus, Int. J. Mod. Phys. C 3 (1992) 1155.

[72] U.H.E. Hansmann, Nucl. Phys. B Proc. Suppl. 30 (1993) 285.

[73] K. Rummukainen, Nucl. Phys. B. Proc. Suppl. 30 (1993) 273.

[74] W. Janke, S. Kappler, Phys. Rev. Lett. 74 (1995) 212.

[75] W. Janke, T. Sauer, Phys. Rev. E 49 (1994) 3475.

[76] W. Janke, Nucl. Phys. B Proc. Suppl. 34 (1994) 771.

[77] W. Janke, J. Stat. Phys. 78 (1995) 759.

[78] B.A. Berg, U.H.E. Hansmann, Y. Okamoto, J. Phys. Chem. 99 (1995) 2236.

[79] U.H.E. Hansmann, Y. Okamoto, F. Eisenmenger, Chem. Phys. Lett. 259 (1996) 321.

[80] M.P. Allen, in: M.P. Allen, D.J. Tildesley (Eds.), Computer Simulation in Chemical Physics, Ch. 4, Kluwer Academic Publishers, Dordrecht, 1993.

[81] In this paper we therefore omit the prefactor $(\Lambda^{3N}N!)^{-1}$ (with the thermal wavelength $\Lambda = \sqrt{h^2/(2\pi m k_B T)}$) of the partition function.

[82] A.M. Ferrenberg, R.H. Swendsen, Phys. Rev. Lett. 61 (1988) 2635.

[83] A.M. Ferrenberg, R.H. Swendsen, Phys. Rev. Lett. 63 (1989) 1195 and 1658(E).

[84] J. Lee, J.M. Kosterlitz, Phys. Rev. Lett. 65 (1990) 137.

[85] Here and in the following we implicitly assume continuous variables. The modification to the case of discrete variables is straightforward. – Note also that the volume V as argument of the volume histogram $\mathscr{P}_{\beta,p}(V)$ is denoted by an italic roman capital, like the ensemble average $\langle \mathscr{V} \rangle$ of the system volume in the isobaric ensemble, although both quantities are conceptually and therefore in general also numerically different. However, the meaning of the symbol V should always be clear from the context.

[86] It should be clear that in any ensemble different from the canonical one (i.e., whenever $\mathscr{H}(x)$ is not the internal energy $\mathscr{U}(x)$) the ensemble average $\langle \mathscr{H} \rangle$ is not the (internal) energy, but an enthalpy-like quantity, which in addition to the internal energy contains further contributions from 'external fields' (magnetic field, chemical potential, etc.). Nevertheless we will term this quantity *the energy* of the system. Likewise the quantity $S(E)$ related to the density of states $\Omega(E)$ of E by $S(E) = k_B \ln \Omega(E)$ will be termed *the entropy* of the system, although it will in general be different from the microcanonical entropy.

[87] R.H. Swendsen, J.-S. Wang, A.M. Ferrenberg, in: K. Binder (Ed.), The Monte Carlo Method in Condensed Matter Physics, Ch. 4, 2nd ed., Springer, Berlin, 1995.

[88] K. Binder, Reps. Prog. Phys. 50 (1987) 783.

[89] This is in contrast to "symmetric" first–order transitions like the transition from positive to negative magnetization in the Ising model at zero magnetic field below T_c, where the two coexisting phases are related by the spin-up/spin-down symmetry. Finite-size scaling results for symmetric first-order phase transitions can be found in: V. Privman (Ed.), Finite–Size Scaling and Numerical Simulation of Statistical Systems, World Scientific, Singapore, 1990; V. Privman, M.E. Fisher, J. Stat. Phys. 33 (1983) 385; K. Binder, D.P. Landau, Phys. Rev. B 30 (1984) 1477; M.E. Fisher, V. Privman, Phys. Rev. B 32 (1985) 447; K. Binder, in: K. Binder (Ed.), Applications of the Monte Carlo Method in Statistical Physics, Ch. 1, 2nd ed., Springer, Berlin, 1987.

[90] M.S.S. Challa, D.P. Landau, K. Binder, Phys. Rev. B 34 (1986) 1841.

[91] C. Borgs, R. Kotecky, J. Stat. Phys. 61 (1990) 79.

[92] C. Borgs, R. Kotecky, S. Miracle-Sole, J. Stat. Phys. 62 (1990) 529.

[93] C. Borgs, S. Kappler, Phys. Lett. A 171 (1992) 37.

[94] K. Binder, in: K. Binder (Ed.), The Monte Carlo Method in Condensed Matter Physics, Ch. 1, 2nd ed., Springer, Berlin 1995, 1977.

[95] Usually the maximum of the specific heat as a function of temperature is chosen as an estimate for the transition temperature $T_t(L)$ of the finite system. In the following we will discuss how an estimate for $T_t(L)$ can alternatively be derived directly from energy histograms.

[96] Note that the 'shifting' of the transition temperature and the 'smearing-out' of the transition are also characteristics of continuous phase transitions. In both cases finite-size scaling theory predicts the L-dependency of the positions and widths of the histogram peaks, although the underlying mechanisms and the resulting scaling laws are quite different.

[97] N. Metropolis, A.W. Rosenbluth, M.N. Rosenbluth, A.H. Teller, E. Teller, J. Chem. Phys. 21 (1953) 1087.

[98] O.G. Mouritsen, Chem. Phys. Lipids 57 (1991) 179.

[99] R.L. Biltonen, J. Chem. Thermodyn. 22 (1990) 1.

[100] O.G. Mouritsen, K. Jørgensen, Chem. Phys. Lipids 73 (1994) 3.

[101] Z. Zhang, M. Laradji, H. Guo, O.G. Mouritsen, M.J. Zuckermann, Phys. Rev. A 45 (1992) 7560.

[102] J. Risbo, M.M. Sperotto, O.G. Mouritsen, J. Chem. Phys. 103 (1995) 3643.

[103] M. Nielsen, L. Miao, J.H. Ipsen, O.G. Mouritsen, M.J. Zuckermann, Phys. Rev. E 54 (1996) 6889.

[104] D.A. Pink, T.J. Green, D. Chapman, Biochemistry 20 (1981) 6692.

[105] O.G. Mouritsen, in: R. Brasseur (Ed.), Molecular Description of Biological Membrane Components by Computer Aided Conformational Analysis, vol. 1, CRC Press, Boca Raton, 1990, p. 3.

[106] K. Jørgensen, M.M. Sperotto, O.G. Mouritsen, J.H. Ipsen, M.J. Zuckermann, Biochim. Biophys. Acta 1152 (1993) 135.

[107] E. Corvera, M. Laradji, M.J. Zuckermann, Phys. Rev. E 47 (1993) 696.

[108] L.E. Murr, Interfacial Phenomena in Metals and Alloys, Addison-Wesley, Reading, MA, 1975, p. 321.

[109] L.K. Fionova, A.V. Artemyev, Grain Boundaries in Metals and Semiconductors, Les Éditions de Physique, Les Ulis Cedex, France, 1993.

[110] S. Dietrich, in: C. Domb, J.L. Lebowitz (Eds.), Phase Transitions and Critical Phenomena, vol. 12, Academic Press, New York, 1988, p. 1.

[111] D.E. Sullivan, M.M. Telo de Gama, in: C.A. Croxton (Ed.), Fluid Interfacial Phenomena, Wiley, New York, 1986, p. 45.

[112] M. Schick, in: J. Charvolin, J.F. Joanny, J. Zinn-Justin (Eds.), Liquids at Interfaces, Elsevier, Amsterdam, 1990, p. 415.

[113] References of experimental studies and of computer simulation studies of model systems exhibiting interfacial melting can be found in Ref. [114].

[114] G. Besold, O.G. Mouritsen, Phys. Rev. B 50 (1994) 6573.

[115] G. Besold, O.G. Mouritsen, to be published.

[116] J. Orban, J. van Craen, A. Bellemans, J. Chem. Phys. 49 (1968) 1778.

[117] K. Müller, G. Besold, K. Heinz, in: H.P. Bonzel, A.M. Bradshaw, G. Ertl (Eds.), Physics and Chemistry of Alkali Adsorption, Elsevier, Amsterdam, 1989, p. 65.

[118] R. Kikuchi, J.W. Cahn, Phys. Rev. B 21 (1980) 1893.

[119] For lattice models without superstructures, like the model for a binary lipid layer discussed in Section 4.1, this effect is in general less apparent.

[120] For the system size $L = 5$ the scattering in the distributions turned out to be so high that an estimate of $T_m(L = 5)$ could not be determined.

[121] G.M. Torrie, J.P. Valleau, J. Comp. Phys. 22 (1977) 187.

[122] G.M. Torrie, J.P. Valleau, J. Comp. Phys. 23 (1977) 187.

[123] J.P. Valleau, G.M. Torrie, in: B.J. Berne (Ed.), Statistical Mechanics Part A: Equilibrium Techniques, Plenum Press, New York London, 1977.